



# Integrated Methane Inversion (IMI) 2.0: an improved research and stakeholder tool for monitoring total methane emissions with high resolution worldwide using TROPOMI satellite observations

Lucas A. Estrada<sup>1</sup>, Daniel J. Varon<sup>1</sup>, Melissa Sulprizio<sup>1</sup>, Hannah Nesser<sup>2</sup>, Zichong Chen<sup>1</sup>, Nicholas Balasus<sup>1</sup>, Sarah E. Hancock<sup>1</sup>, Megan He<sup>1</sup>, James D. East<sup>1</sup>, Todd A. Mooring<sup>3</sup>, Alexander Oort Alonso<sup>1</sup>, Joannes D. Maasakkers<sup>4</sup>, Ilse Aben<sup>4</sup>, Sabour Baray<sup>5</sup>, Kevin W. Bowman<sup>2</sup>, John R. Worden<sup>2</sup>, Felipe J. Cardoso-Saldaña<sup>6</sup>, Emily Reidy<sup>6</sup>, Daniel J. Jacob<sup>1</sup>

<sup>1</sup>School of Engineering and Applied Science, Harvard University, Cambridge, Massachusetts, USA

<sup>2</sup>Jet Propulsion Laboratory, California Institute of Technology, Pasadena, California, USA

10 <sup>3</sup>Department of Earth and Planetary Sciences, Harvard University, Cambridge, MA, USA

<sup>4</sup>SRON Netherlands Institute for Space Research, Leiden, the Netherlands

<sup>5</sup>Environment and Climate Change Canada, Toronto, ON, Canada

<sup>6</sup>ExxonMobil Technology and Engineering Company, Spring, TX, USA

*Correspondence to:* Lucas A. Estrada (lestrada@g.harvard.edu)

15 **Abstract.** Satellite observations of atmospheric methane are a powerful resource for helping to quantify methane emissions in service of climate action. The inverse methods needed to exploit these observations require a high level of scientific and technical expertise as well as access to large computational and data processing resources. The Integrated Methane Inversion (IMI) is an open-access cloud computing tool designed for researchers and non-expert users to obtain total sector-resolved methane emissions worldwide at up to  $0.25^\circ \times 0.3125^\circ$  ( $\approx 25 \times 25$  km<sup>2</sup>) resolution by analytical inversion of TROPOMI satellite  
20 observations with closed-form error characterization. Here we describe IMI version 2.0 with vastly expanded capabilities relative to the original version. Major developments include: (i) a new blended TROPOMI+GOSAT dataset for higher data quality, (ii) incorporation of point source observations in state vector construction, (iii) order-of-magnitude speedup in Jacobian matrix construction, (iv) improved error characterization through use of super-observations, (v) improved methods  
25 to optimize tropospheric OH (main methane sink), (viii) global inversion capability, (ix) Kalman filter option for continuous monitoring of emissions, (x) updated default prior emission inventories, (xi) option for lognormal error probability density functions to characterize emissions, (xii) additional output visualization (sectoral emissions, temporal variability), and (xiii) containerization to facilitate download to local computing facilities and operation as part of the US GHG Center. A 2023 annual inversion with 28-day temporal resolution for the contiguous US (CONUS) is presented as demonstration of IMI 2.0  
30 capabilities.



## 1 Introduction

Methane, a powerful greenhouse gas, has become a top policy concern for mitigating anthropogenic climate change. Its short atmospheric lifetime (~9 years) and high warming effect (~82 times the global warming potential of CO<sub>2</sub> for a 20-year period) make reducing methane emissions an attractive option for yielding near-term climate benefits (Naik et al., 2013; Forster et al., 2021). Over 150 countries have joined the Global Methane pledge, committing to collectively reduce global methane emissions 30% by 2030 (Global Methane Pledge, 2023). Despite the recent attention from policymakers, global atmospheric concentrations of methane continue to rise rapidly, at a rate of 0.8% per year for 2020-2022 (Thoning et al., 2022). Quantification and monitoring of methane emissions from different sectors worldwide and with high resolution is crucial for understanding methane trends and developing mitigation methods to achieve policy goals.

40

Methane has anthropogenic sources from many sectors including livestock, oil and gas operations, coal mining, landfills, wastewater treatment, and rice cultivation (Saunio et al., 2020). Wetlands are the dominant natural source. Emissions are estimated using either bottom-up or top-down methods. Bottom-up methods apply emission factors to units of activity, but these emission factors can have large uncertainties and activity data may lag by several years. Top-down methods use observations of atmospheric methane combined with an atmospheric transport model to infer emissions, but there may be errors in the observations and in the modeling of transport. Inversions of atmospheric observations blend these two methods by using bottom-up estimates as prior information and adjusting them to optimize the fit to observations through the atmospheric transport model, with formal characterization of errors by Bayesian synthesis (Brasseur and Jacob, 2017). Results from these inversions can provide guidance for improving policy-relevant bottom-up inventories.

50

Satellite observations of atmospheric methane have greatly increased the potential of inverse analyses by providing global continuous coverage and high data density. Satellites retrieve methane dry column mixing ratios  $X_{CH_4}$  with sensitivity down to the surface by measuring backscattered solar radiation in the shortwave infrared (SWIR) (Jacob et al., 2016). Observations are available from a range of satellite instruments to quantify emissions from the global scale down to point sources (Jacob et al., 2022). The TROPOMI instrument launched in October 2017 has daily global coverage with  $5.5 \times 7$  km<sup>2</sup> nadir pixel resolution (Veefkind et al., 2012; Lorente et al., 2021) and presently provides the most spatially dense top-down resource for global mapping of total methane emissions. A number of inverse studies have used TROPOMI observations to quantify methane emissions globally and for specific regions (Cusworth et al., 2020; Y. Zhang et al., 2020; McNorton et al., 2022; Chen et al., 2023; Li et al., 2023; Naus et al., 2023; Shen et al., 2023; Tsuruta et al., 2023; Varon et al., 2023; Yu et al., 2023; Nesser et al., 2024). Point source imagers including GHGSat, EMIT, PRISMA, and Sentinel-2 provide individual information on large point sources (Jacob et al., 2022).

60



65 Inversions of satellite data require a high level of technical and scientific expertise, as well as large computational and data processing resources. Transparency and accessibility of the methods are essential for making the resulting emission estimates actionable by stakeholders. These stakeholders may be from government agencies at all levels (municipal to national), international agencies, non-governmental organizations, industry, and advocacy groups. Greater impact can be achieved if the methods are usable by the stakeholders themselves. New inversion tools have recently been developed for this purpose including the Community Inversion Framework (Berchet et al., 2021) and version 1.0 of the Integrated Methane Inversion (IMI; Varon et al., 2022).

70

The IMI (<https://imi.seas.harvard.edu>) is specifically designed to enable researchers and non-expert stakeholders to exploit TROPOMI satellite data for optimizing total methane emission estimates at up to 25-km resolution. It uses a state-of-the-art analytical inversion method with closed-form error characterization documented in the research literature. It operates on the Amazon Web Services (AWS) cloud, where both TROPOMI data and the atmospheric transport model (GEOS-Chem) reside, thus avoiding the need for local computing resources and instead bringing compute to data. The IMI has a user-friendly interface to enable stakeholders to optimize emission estimates for any selected domain and period through a configuration file, with default or user-defined prior estimates and error specifications. It features an open-source codebase, comprehensive documentation (<https://imi.readthedocs.io/en/latest/>), and frequent versioning to keep the methods up to date with current research. The IMI is actively being used for research applications (Baray et al., 2023; Chen et al., 2023; Nathan et al., 2023; Varon et al., 2023; Hancock et al., 2024; Hemati et al., 2024).

80

Varon et al. (2022) documented the initial release of IMI 1.0, limited at the time to regional inverse analyses of TROPOMI observations with  $0.25^{\circ} \times 0.3125^{\circ}$  ( $\approx 25 \times 25$  km<sup>2</sup>) or  $0.5^{\circ} \times 0.625^{\circ}$  ( $\approx 50 \times 50$  km<sup>2</sup>) resolution. Since then, the IMI has undergone substantial development, and we document here the greatly enhanced capabilities of IMI 2.0 including the major new features listed in Table 1. These IMI 2.0 advancements improve the overall flexibility of the IMI for a wider range of scientific and stakeholder applications from regional to global scales and with low temporal latency to enable continuous monitoring. Sect. 2 gives a summary description of IMI 1.0 and Sect. 3 describes the major new features of IMI 2.0. A 1-year demo inversion for the contiguous US (CONUS) is presented in Sect. 4.

90

95



**Table 1: Integrated Methane Inversion (IMI) capabilities**

IMI 1.0 (Varon et al., 2022)	IMI 2.0 New Capabilities <sup>a</sup>
<ul style="list-style-type: none"> <li>• Emission optimization for regional domains with 25-50 km resolution by analytical inversion of TROPOMI observations</li> <li>• Smoothed TROPOMI fields as boundary conditions</li> <li>• Open-source code on AWS cloud with user-friendly interface</li> <li>• IMI preview for visualizing data and assessing information content before performing inversion.</li> <li>• Output data and imagery for posterior (optimized) fluxes with error statistics</li> </ul>	<ol style="list-style-type: none"> <li>1. Blended TROPOMI+GOSAT dataset compatibility</li> <li>2. Point source incorporation in state vector construction</li> <li>3. Jacobian matrix construction speed-up</li> <li>4. Super-observations</li> <li>5. Optimization of boundary conditions</li> <li>6. Adaptive information-based spatial resolution</li> <li>7. Optimization of methane sink from OH</li> <li>8. Global inversion capability</li> <li>9. Low-latency emission updates (continuous monitoring)</li> <li>10. New bottom-up emission inventories as prior estimates</li> <li>11. Lognormal error statistics for prior emission estimates</li> <li>12. Enriched output information</li> <li>13. Docker container for code download to local systems</li> </ol>

<sup>a</sup>Numbers correspond to subsections in Sect. 3.

## 2 Integrated Methane Inversion (IMI) 1.0

We start with a summary description of the Integrated Methane Inversion (IMI) 1.0, previously described by Varon et al. (2022), to provide context for the new developments in IMI 2.0. IMI is designed as an open-source software tool for use on the cloud or local clusters to infer methane emissions from TROPOMI satellite observations using GEOS-Chem as the forward atmospheric transport model. The TROPOMI data are from the latest operational retrieval version archived on the AWS cloud (currently v02.06.00; Lorente et al., 2023). The data are filtered to remove retrievals with QA value  $\leq 0.5$ , water pixels, and pixels south of 60°S. GEOS-Chem is a global 3-D chemical transport model (Wecht et al., 2014) that can operate in regional mode at up to 0.25°×0.3125° resolution using archived meteorological input from the NASA Goddard Earth Observing System - Fast Processing (GEOS-FP) and MERRA-2 datasets. The IMI uses GEOS-Chem Classic with shared-memory parallelization (Bey et al., 2001). Smoothed TROPOMI fields are used as GEOS-Chem boundary conditions to ensure consistency with the TROPOMI data within the inversion domain (Shen et al., 2021).

IMI 1.0 conducts methane inversions on the native 0.25°×0.3125° GEOS-FP grid (or alternatively the 0.5°×0.625° MERRA-2 grid) over the TROPOMI record from May 2018 to present. Users perform methane inversions by filling out a simple configuration text file (YAML format) selecting their region and period of interest. The region can be set as a rectilinear domain (latitude and longitude boundaries) or by providing a shapefile with any geometry. The state vector optimized by the



inversion consists of temporal mean emissions for the period of interest in individual emitting grid cells (including offshore  
115 emissions) within the region of interest, plus buffer clusters surrounding the region of interest to correct boundary  
conditions. Prior estimates for the inversion are from a default IMI library of bottom-up emission inventories, but users can  
substitute their own. The cloud compatibility of the IMI allows users to leverage the vast computation resources of the AWS  
cloud for performing inversions without need for a local compute cluster. It takes advantage of input data already being  
resident on the cloud including the TROPOMI observations, the smoothed TROPOMI fields used as boundary and initial  
120 conditions for the inversions, the GEOS-FP and MERRA-2 meteorological datasets used by GEOS-Chem, and the bottom-  
up emission inventories as prior estimates. Advanced users can adjust the inversion settings via the configuration file or  
through manual update of the inversion workflow, which involves a collection of Bash™ and Python® scripts.

The IMI follows the established Bayesian analytical inversion technique described by Brasseur and Jacob (2017) to optimize  
125 an emission state vector  $\mathbf{x}$  (2-D gridded fluxes) by minimizing the cost function  $J(\mathbf{x})$ :

$$J(\mathbf{x}) = (\mathbf{x} - \mathbf{x}_A)^T \mathbf{S}_A^{-1} (\mathbf{x} - \mathbf{x}_A) + \gamma (\mathbf{y} - \mathbf{K}\mathbf{x})^T \mathbf{S}_o^{-1} (\mathbf{y} - \mathbf{K}\mathbf{x}) \quad (1)$$

Here  $\mathbf{x}_A$  is the prior estimate,  $\mathbf{y}$  denotes the observations assembled into a vector,  $\mathbf{S}_A$  is the prior error covariance matrix,  $\mathbf{S}_o$   
is the error covariance matrix of the observational system,  $\mathbf{K}$  is the Jacobian matrix describing the forward model sensitivity  
of the observations to perturbations in emissions, and  $\gamma \in [0,1]$  is a regularization parameter to compensate for unaccounted  
130 error covariances in the observational system (Lu et al., 2021). The optimized emissions  $\hat{\mathbf{x}}$  (posterior estimate) are obtained  
by solving analytically for the cost function minimum where  $\partial J / \partial \mathbf{x} = 0$ :

$$\hat{\mathbf{x}} = \mathbf{x}_A + (\gamma \mathbf{K}^T \mathbf{S}_o^{-1} \mathbf{K} + \mathbf{S}_A^{-1})^{-1} \gamma \mathbf{K}^T \mathbf{S}_o^{-1} (\mathbf{y} - \mathbf{K}\mathbf{x}_A) \quad (2)$$

The relationship of emissions to concentrations is linear so that  $\mathbf{K}$  fully defines the forward model for the purpose of the  
135 inversion. It is constructed column by column by running embarrassingly parallel perturbation simulations with the GEOS-  
Chem forward model.

A major advantage of the analytical solution is that it provides a closed-form expression for the posterior error covariance  
matrix  $\hat{\mathbf{S}}$ :

140

$$\hat{\mathbf{S}} = (\gamma \mathbf{K}^T \mathbf{S}_o^{-1} \mathbf{K} + \mathbf{S}_A^{-1})^{-1} \quad (3)$$



$\hat{\mathbf{S}}$  characterizes the error on  $\hat{\mathbf{x}}$ , and comparison to  $\mathbf{S}_A$  quantifies the information content from the inversion. This is critically important for satellite observations, which generally do not fully constrain the state vector. From  $\hat{\mathbf{S}}$  we derive the averaging kernel matrix  $\mathbf{A} = \partial \hat{\mathbf{x}} / \partial \mathbf{x} = \mathbf{I} - \hat{\mathbf{S}}\mathbf{S}_A^{-1}$ , which measures the sensitivity of the inverse solution to the true state. The trace of  $\mathbf{A}$  measures the degrees of freedom for signal (DOFS), representing the number of independent pieces of information on the state vector obtained from the inversion, and the diagonal elements  $a_{ii} = \partial \hat{x}_i / \partial x_i \in [0,1]$  measure the ability of the inversion to quantify state vector element  $x_i$  independently from the prior estimate (fully if  $a_{ii} = 1$ , not at all if  $a_{ii} = 0$ ). Another advantage of the analytical solution is that once  $\mathbf{K}$  has been constructed, any ensemble of analytical inversions exploring the sensitivity to different inversion parameters can be easily generated (Chen et al., 2022).

Regional inversions require unbiased boundary conditions, as biases in boundary conditions would propagate to the optimized emissions in the inversion domain. The IMI maintains a global 3-D archive of bias-corrected GEOS-Chem fields (called smoothed TROPOMI fields) to serve as unbiased boundary conditions for any TROPOMI inversion domain or period. The archive is produced by correcting a global continuous GEOS-Chem simulation at  $4^\circ \times 5^\circ$  resolution with smoothed TROPOMI concentrations ( $12^\circ \times 15^\circ$  spatially and  $\pm 15$  days temporally) and applying zonal mean corrections over the oceans. In IMI 1.0, boundary conditions are further corrected in the inversion using buffer grid cell clusters surrounding the region of interest (Shen et al., 2021).

The IMI includes a preview feature to quickly estimate the information content and computational cost of a proposed inversion before investing resources in running the full inversion. The preview provides maps of mean TROPOMI concentrations, observation density, prior emissions, estimated averaging kernel sensitivities, and SWIR albedo for the selected inversion period and domain, along with a cost estimate for running on the cloud. The averaging kernel sensitivities  $a_{ii}$  and  $\text{DOFS} = \sum_i a_{ii}$  are estimated without doing the actual inversion by assuming uniform observations and a simple transport parameterization:

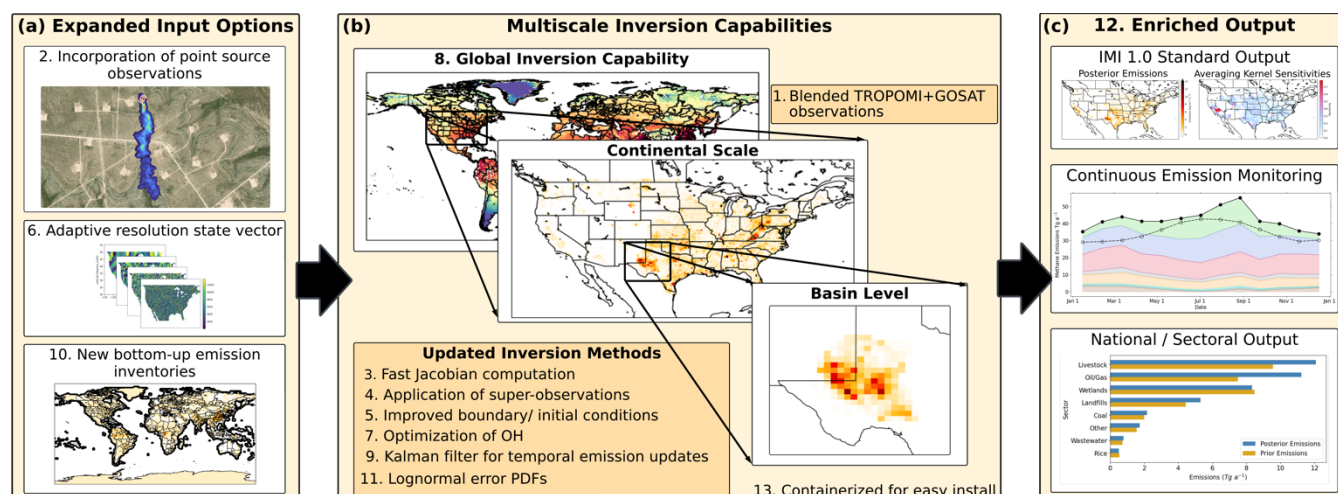
$$a_{ii} = \frac{\sigma_{a_i}^2}{\sigma_{a_i}^2 + \frac{(\sigma_o/k)^2}{m/n}}, \quad (4)$$

where  $\sigma_{a_i}$  is the prior error standard deviation for  $x_{a_i}$ ,  $\sigma_o$  is the observational error standard deviation,  $m$  is the number of satellite observations in the domain,  $n$  is the number of state vector elements, and  $k$  relates  $X_{\text{CH}_4}$  to local emissions with a simple advection-diffusion formulation (Nesser et al., 2021). The estimated DOFS measures how well an inversion with the specified configuration will be able to quantify emissions and allows the users to modify their inversion domain and/or period to improve this ability.



The IMI has extensive documentation available through its website (<https://imi.seas.harvard.edu>). The source code has undergone incremental development since 1.0 with official releases of IMI 1.1 and 1.2 and has an international following of users. Version 2.0 described here represents a transformational leap in the capabilities of the IMI.

### 3 New features in IMI 2.0



180 **Figure 1: Summary of major new features in IMI 2.0 divided into three categories: (a) expanded input options, (b) multiscale inversion capabilities, and (c) enriched output. Numbering of individual features corresponds to the relevant subsection in Sect. 3. Methane plume map in the top left panel is from Carbon Mapper (Methane Dashboard | Carbon Mapper, 2024).**

IMI 2.0 improves IMI 1.0 on a number of fronts including accuracy, performance, capability, and versatility for scientific and stakeholder applications. Table 1 lists the principal features, and these are illustrated in Fig. 1. The following subsections elaborate on each feature in the numerical order of the Table. IMI 2.0 gives users the option of a new blended TROPOMI+GOSAT dataset removing most artifacts from the operational product (Sect. 3.1). It automatically downloads information on large point sources (Sect. 3.2). Computational performance is improved several-fold through fast construction of the Jacobian matrix (Sect. 3.3) and through use of super-observations that also better account for observational error correlation (Sect. 3.4). Boundary/initial conditions are improved, including synchronous representation of the stratosphere, and allowing for boundary condition optimization through the inversion (Sect. 3.5). The capability to conduct inversions over large domains is enhanced by an adaptive k-means clustering scheme (Sect. 3.6). The methane sink from oxidation by tropospheric OH can be optimized (Sect. 3.7). Inversions can be conducted on the global scale (Sect. 3.8). IMI 2.0 features a new capability for time-dependent inversions, allowing continuous monitoring of the evolution of emissions over a selected region of interest (Sect. 3.9). New prior emission inventories are introduced (Sect. 3.10). Users can



195 select lognormal error probability density functions (PDFs) for prior emissions to resolve the heavy tail in the distribution  
 (Sect. 3.11). The inversion output includes new national and sectoral information on posterior emission estimates as well as  
 time series visualizations (Sect. 3.12). The IMI is now in a software container to facilitate downloads to local computing  
 clusters (Sect. 3.13). Most improvements in IMI 2.0 are the heritage of research studies referenced in the appropriate  
 subsections.

200

Table 2 gives a summary list of the user-controlled variables in the IMI 2.0 configuration file. Full documentation is at  
<https://imi.readthedocs.io>. The default settings enable a basic user to run the IMI as simply as specifying a rectilinear  
 inversion domain and time period. More advanced users have a wide range of options. The last column lists the settings used  
 in the US demo inversion of Sect. 4.

205

**Table 2: IMI 2.0 configuration variables <sup>a</sup>**

Setting	Default	Options	US demo (Sect. 4)
Spatial domain	Regional rectilinear <sup>b</sup>	Shapefile or global	CONUS shapefile
Time period	Start and end dates	Continuous monitoring	Jan 1 – Dec 31, 2023
Spatial resolution	0.25°×0.3125°	0.5°×0.625°, 2°×2.5°, 4°×5°	0.25°×0.3125°
Observation dataset	TROPOMI	Blended TROPOMI+GOSAT	Blended TROPOMI+GOSAT
Over water observations	No	Yes	No
Point source datasets <sup>c</sup>	SRON	Carbon Mapper, IMEO	SRON
Temporal updates (Kalman filter)	No	Yes <sup>d</sup>	Yes
State vector dimension	Native resolution	Clustering <sup>e</sup>	Clustering <sup>f</sup>
Country tag <sup>g</sup>	No	Yes	Yes
Jacobian construction grouping <sup>h</sup>	5	Any positive number	5
Boundary condition optimization <sup>i</sup>	Yes	No	Yes
OH optimization <sup>j</sup>	No	Yes	No
Prior emission inventories	Table 3	Other inventories	Table 3
Prior error PDFs <sup>k</sup>	Normal	Lognormal	Normal
Prior error standard deviation	0.5 <sup>l</sup>	Any value	0.5
Observational error, ppb <sup>m</sup>	15	Any positive number	15
Regularization parameter $\gamma$	1.0	Any positive number	0.2

<sup>a</sup> Full documentation is at <https://imi.readthedocs.io>.

<sup>b</sup> Defined by latitude/longitude boundaries.

<sup>c</sup> To impose native resolution in the inversion for locations of detected large point sources. Includes option to only include point sources above a certain  
 value (default set to 2500 kg h<sup>-1</sup>) and/or above a threshold of repeat observations (default 50).

<sup>d</sup> With choices for the update frequency (e.g. 1-week/ 1-month) and specification of the nudge factor, which is the percent weight of the original prior  
 emissions to apply to the prior in the next inversion interval. See Sect. 3.9 and Varon et al. (2023) for more details.

210





- 215 <sup>e</sup> k-means information-based clustering to reduce state vector size with default or user-set parameters and including adaptive capability in Kalman filter mode (Sect. 3.6). Users can adjust cluster size distribution by setting the maximum cluster size (default 64 grid cells) and a threshold for information content per cluster (default of DOFS/ $n$  from the IMI preview).
- <sup>f</sup> With specification of 600 state vector elements.
- <sup>g</sup> Used in k-means clustering algorithm to contain individual clusters within national borders, and also for national output of emissions by sectors.
- <sup>h</sup> Number of state vector elements perturbed (columns of Jacobian matrix constructed) in each GEOS-Chem simulation, chosen to balance CPU time and wall time (Sect. 3.3).
- 220 <sup>i</sup> Setting ignored in global inversions. Error standard deviation configured by user with default of 10 ppb.
- <sup>j</sup> Optimization of domain mean (regional inversions) or hemispheric mean (global inversions) tropospheric OH concentrations expressed as methane loss frequencies and with user-adjustable default error standard deviation of 10%.
- <sup>k</sup> For prior emission estimates.
- <sup>l</sup> Fractional error standard deviation for a normal error PDF, geometric standard deviation for a lognormal error PDF.
- 225 <sup>m</sup> Error standard deviation for individual observations. including contributions from measurement, retrieval, representation, and forward model errors.

### 3.1 Blended TROPOMI+GOSAT dataset

TROPOMI observations are available from May 2018 to present. The current TROPOMI operational retrieval is posted with 2-3 day latency on the AWS cloud (presently version 02.06.00; Sentinel-5P Level 2 - Registry of Open Data on AWS, 2024; Lorente et al., 2023) and is accessed there by the IMI as default. The retrieval is regularly updated to resolve artifacts from surface albedo, aerosols, clouds, and cross-track detector differences (Lorente et al., 2023). We also provide an option to use the blended TROPOMI+GOSAT dataset of Balasus et al. (2023), which applies machine learning to correct the TROPOMI version 02.06.00 retrieval with the more accurate but much sparser retrieval from the GOSAT satellite instrument (Parker et al., 2020). Glint observations over water were previously filtered out due to high biases and artifacts in the TROPOMI retrieval, but with the higher fidelity of the blended TROPOMI+GOSAT dataset we include an option to include these observations in the inversion. The blended TROPOMI+GOSAT data are available on the AWS cloud for the full duration of the TROPOMI record and we keep them current for use in the IMI. Comparison of the blended TROPOMI+GOSAT and operational TROPOMI datasets through the IMI preview can be insightful for identifying retrieval artifacts.

### 3.2 Point source incorporation in the state vector construction

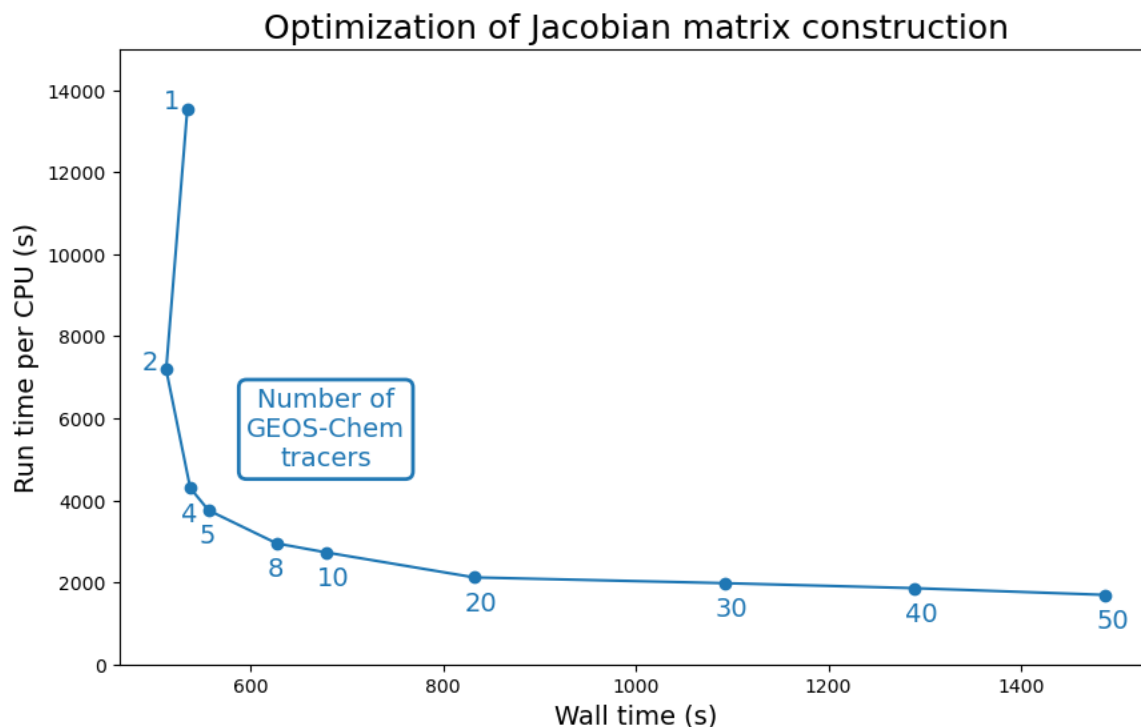
240 We refer to point sources as emissions over 100 kg h<sup>-1</sup> from individual facilities. Point source satellite imagers with high spatial resolution are variably able to detect plumes from individual point sources and quantify emissions, but integrating this growing dataset into inversions is challenging due to uncertainties in point source observability, variability, and persistence (Cardoso-Saldaña and Allen, 2020; Cusworth et al., 2020; Watine-Guiu et al., 2023). Possible methods include enforcing high state vector resolution where point sources have been observed (Chen et al., 2023), introducing additional point source state vector elements (Naus et al., 2023), and using point source data to evaluate posterior results in a TROPOMI-only inversion (Cusworth et al., 2020). Here, we integrate point source information into the IMI when constructing a reduced state vector (Sect. 3.6) by enforcing native resolution for state vector elements with point sources above a specified threshold in the continually updated global datasets from SRON (Schuit et al., 2023; Methane Plume Maps, 2024), IMEO (International Methane Emissions Observatory, 2024), and Carbon Mapper (Cusworth et al., 2024). These datasets include point source



250 information from Sentinel-2/3/5, EMIT, PRISMA, EnMAP, GOES, and Landsat-8/9. Point source locations are included as  
an overlay on the prior emission maps in the IMI preview.

### 3.3 Fast Jacobian construction

Construction of the Jacobian matrix,  $\mathbf{K}$ , is the most computationally expensive component of the IMI and has previously  
limited the size of the state vector to  $\sim 2,000$  elements.  $\mathbf{K}$  is constructed column by column by conducting GEOS-Chem  
255 simulations over the inversion time period perturbing individual state vector elements and collecting the resulting changes in  
concentrations. This was done in IMI 1.0 with separate GEOS-Chem simulations for each state vector element, and  
additional overhead was incurred by compiling methane emissions in GEOS-Chem with the Harmonized Emission  
Component (HEMCO; Lin et al., 2021). For IMI 2.0 we made several improvements to our Jacobian construction practices.  
To avoid the effect of small nonlinearities in the advection code (Lin and Rood, 1996), we construct our Jacobian columns  
260 by specifying a low methane background and initial conditions (1 ppb), applying a high perturbation to the emission state  
vector element of interest ( $10^{-8} \text{ kg m}^{-2} \text{ s}^{-1}$ ), and setting all other emission state vector elements to zero. To improve  
computational performance, we modified GEOS-Chem to simulate multiple methane species as separate transported tracers,  
so that several columns of the Jacobian can be constructed at once with no additional overhead, and we precompile the  
emissions with HEMCO, reducing the time to read in emissions. Running GEOS-Chem with a large number of tracers can  
265 increase wall time, because GEOS-Chem Classic simulations are limited to a single node (shared-memory parallelization),  
while multiple GEOS-Chem simulations for Jacobian construction can be spread across nodes. We optimized the number of  
tracers per GEOS-Chem simulation to balance the total CPU time (which decreases with the number of tracers) and the wall  
time (which increases with the number of tracers, because the IMI then uses fewer compute nodes). Tests on the Harvard  
supercomputing cluster using 32 CPUs per GEOS-Chem simulation indicate an optimum of 5 tracers per simulation (Fig. 2).  
270 This yields a  $5\times$  speed-up in the construction of the Jacobian matrix relative to single-tracer simulations in total compute  
hours, traded against a 60% increase in wall time, as shown in Fig. 2. Precompiling emissions with HEMCO yields an  
additional  $2\times$  speed-up, for an overall  $10\times$  decrease in CPU cost and a net decrease in wall time. Users with a large number  
of available nodes can reduce wall time at the expense of CPU time by choosing fewer tracers per simulation as specified in  
the configuration file (Table 2).



275

**Figure 2: Performance optimization of the number of state vector elements (transported methane tracers) in GEOS-Chem simulations used to construct the Jacobian matrix for the IMI. The plot shows the run time per CPU and the total wall time for GEOS-Chem simulations conducted with different numbers of transported tracers. A simulation with 5 tracers (elbow of the curve) provides the optimal performance for CPU and wall time. Tests were done on the Harvard supercomputer cluster for 1-month GEOS-Chem simulations with 32 CPUs (Intel 8480+ processors) at  $0.25^\circ \times 0.3125^\circ$  resolution.**

280

### 3.4 Super-observations

IMI 2.0 uses super-observations as the TROPOMI observation vector  $\mathbf{y}$  in the inversion, following the work of Chen et al. (2023). Super-observations average all individual TROPOMI observations for a given GEOS-Chem grid cell and TROPOMI orbit. Loss of information in this averaging of individual observations is negligible because GEOS-Chem model values are the same for all observations in a common grid cell and time, and retrieval averaging kernels are similar. Using super-observations reduces the storage size and computational time associated with performing the inversion step of the IMI by reducing the dimension of  $\mathbf{y}$ . Additionally, it provides a better characterization of observational error correlations to avoid overfit in the inversion. Using individual observations in the inversion with a diagonal observational error correlation matrix assumes that errors in individual observations are uncorrelated. In fact, transport errors for individual TROPOMI observations within a GEOS-Chem grid cell are perfectly correlated, and retrieval errors may be correlated as well. Using the residual error method (Heald et al., 2004), Chen et al. (2023) derived the observational error variance  $\sigma_{super}^2$  for a super-observation averaging  $P$  individual TROPOMI observations:

290



$$\sigma_{super}^2 = \sigma_{retrieval}^2 \left( \frac{1 - r_{retrieval}}{P} + r_{retrieval} \right) + \sigma_{transport}^2 \quad (5)$$

where  $\sigma_{transport}^2$  is the error variance associated with GEOS-Chem transport,  $\sigma_{retrieval}^2$  is the single retrieval error variance, and  $r_{retrieval}$  is the error correlation coefficient for the  $P$  observations being averaged. We use  $r_{retrieval} = 0.55$  and  $\sigma_{transport} = 4.5$  ppb following Chen et al. (2023), for an inversion at  $0.25^\circ \times 0.3125^\circ$  resolution.  $\sigma_{retrieval}$  is set by the user, with a default value of 15 ppb from previous applications of the residual error method to TROPOMI data (Qu et al., 2021; Shen et al., 2021; Chen et al., 2023). The improved observational error characterization from using super-observations reduces our reliance on  $\gamma$  to account for overfit, allowing  $\gamma$  to be set closer to 1.

### 3.5 Smoothed TROPOMI fields as boundary and initial conditions

It is critical for the IMI to use unbiased initial and boundary conditions (IC/BCs), because bias will otherwise propagate to the emission correction. IMI 1.0 used an archive of spatially and temporally smoothed TROPOMI fields as IC/BCs to avoid systematic bias, and further optimized buffer clusters around the region of interest to correct for BC errors (Sect. 2). In IMI 2.0 we make three updates to the treatment of IC/BCs. First, we improve the process for generating smoothed TROPOMI fields to include a more accurate and synchronous stratosphere (Mooring et al., 2024). Second, we produce an additional parallel archive of smoothed fields for the blended TROPOMI+GOSAT product (Balasus et al., 2023). Third, we allow for the optimization of BCs as well as buffer clusters. Fourth, we conduct the smoothing backward in time (rather than centered in time) to allow for near-real-time (low-latency) applications. The archives of smoothed TROPOMI fields for both the operational product and the blended product are kept current with 2-3 day latency synchronously with the TROPOMI data.

To produce the smoothed TROPOMI archives, we start from a global GEOS-Chem simulation (version 14.3.1) at horizontal resolution of  $2^\circ \times 2.5^\circ$  with 47 vertical layers extending to 0.01 hPa. The simulation uses the default prior emission estimates for the IMI (Table 3). It starts on April 1, 2018 (one month before the start of the TROPOMI record) with ICs from a separate GEOS-Chem simulation initialized in 1985 (Mooring et al., 2024). This multidecadal spin-up simulation uses monthly kriged global surface observations of methane concentrations from the NOAA GLOBALVIEW flask dataset as BCs (Murray, 2016). GEOS-Chem transports these surface BCs throughout the atmosphere, a process that takes years for the stratosphere (Chabrillat et al., 2018). In this manner, we create an April 1, 2018 IC that is consistent with both long-term trends in tropospheric methane and stratospheric transport (Mooring et al., 2024).

The 3-D methane concentration fields from our emissions-driven global simulation starting on April 1, 2018 from this unbiased synchronized atmosphere are archived every 3h from 1 April 2018 until present. We correct these fields to the TROPOMI satellite observations to generate the smoothed TROPOMI fields. For each observation, we apply the TROPOMI operator, which describes the sensitivity of the observation to different vertical levels, to the co-located GEOS-Chem vertical

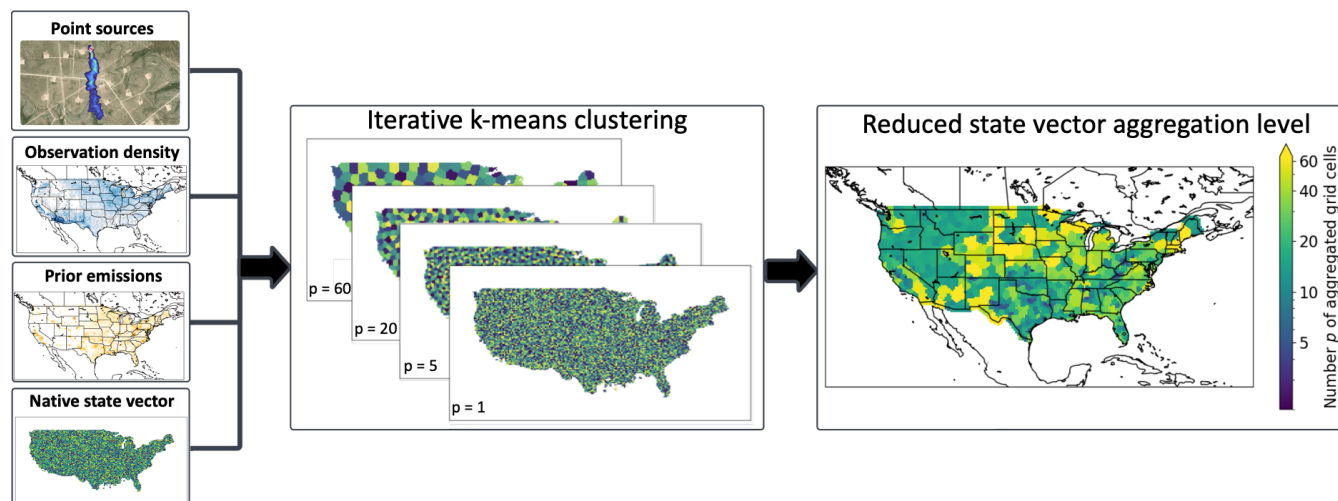


profile, giving us pairs of TROPOMI  $X_{\text{CH}_4}$  and simulated GEOS-Chem  $X_{\text{CH}_4}$ . We average these  $X_{\text{CH}_4}$  values on a  $2^\circ \times 2.5^\circ$   
325 daily grid and subtract them to get a GEOS-Chem column bias  $\Delta X_{\text{CH}_4} = X_{\text{CH}_4, \text{GEOS-Chem}} - X_{\text{CH}_4, \text{TROPOMI}}$ . The column-bias  
fields are then smoothed with a rolling average spatially to  $10^\circ \times 12.5^\circ$  and temporally to 15 days back in time. If there are no  
observations for the past 15 days, we extend the temporal smoothing to 30 days. For grid cells with no column-bias  
information after smoothing (such as over open oceans or high latitudes in the winter), we use a zonal average of the column  
bias for that latitude band. The resulting  $2^\circ \times 2.5^\circ$  daily smoothed column-bias fields are removed from each of the 47 layers  
330 to yield the bias-corrected 3-D GEOS-Chem fields (called smoothed TROPOMI fields) used as IC/BCs in the inversions.

Although our smoothed TROPOMI fields are intended to avoid systematic IC/BC bias in inversions of TROPOMI data,  
there may still be error in the BCs not captured by the smoothing. In IMI 1.0 this was corrected by optimizing emissions in  
buffer clusters surrounding the region of interest. In IMI 2.0 we implement a new option to allow optimization of the BCs as  
335 part of the inversion. When enabled, BC optimization adds four additional elements to the state vector, one for each edge of  
the GEOS-Chem domain (when using a custom shapefile the domain is padded to be rectilinear). Each edge is then  
optimized as part of the inversion, applying a correction factor for the entire considered inversion interval. Optimization of  
BCs can be done in place of or in addition to optimization of buffer clusters.

### 3.6 Adaptive state vector clustering

340 The maximum resolution of the IMI is set by the native  $0.25^\circ \times 0.3125^\circ$  grid cell resolution of the GEOS-Chem forward  
model. Optimizing emissions at such a high resolution through individual state vector elements may be computationally  
burdensome for large domains and may not be justified by the information content of the observations. We introduce in IMI  
2.0 an adaptive k-means clustering algorithm following Nesser et al. (2021) that clusters individual grid cells on the basis of  
proximity and information content. This maintains high resolution in areas of high emissions and dense observations while  
345 smoothing the solution in areas with weak emissions or insufficient observations. The algorithm is adaptive in determining  
the best clustering to apply given user specification of a desired number of state vector elements and minimum resolution,  
and also in adjusting to changing observing conditions for temporally resolved inversions (Sect. 3.9). It is interactive with  
the user through the IMI preview. Users have options to exclude selected grid cells from the clustering (force them to remain  
at native resolution), on the basis of, for example, ancillary observations of large point sources (Sect. 3.2). To improve  
350 national emission accounting, users also have the option to ensure that clusters respect country boundaries.



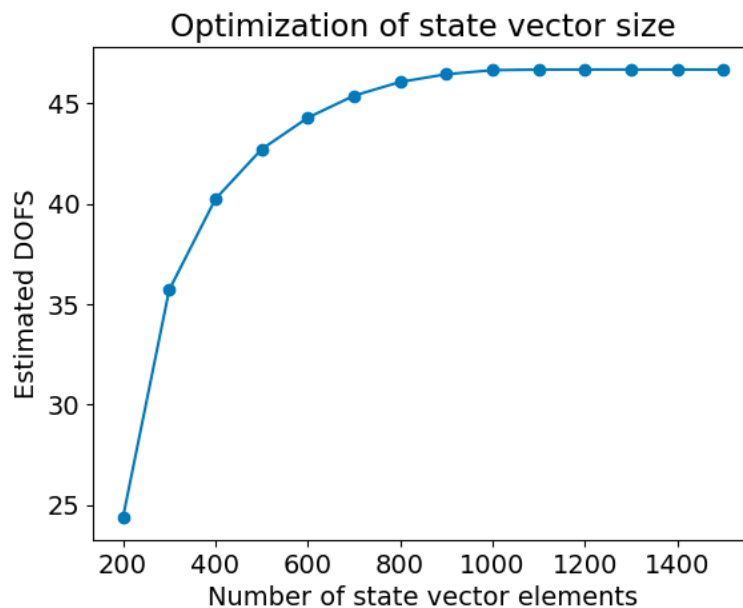
355 **Figure 3: Spatial clustering of state vector elements in IMI 2.0 using iterative k-means and illustrated for the CONUS**  
**emission state vector in the demo of Sect. 4. The native-resolution state vector, consisting here of  $0.25^\circ \times 0.3125^\circ$  grid**  
**cells, is transformed into an ensemble of multi-sized state vector elements aggregating  $p$  grid cells depending on**  
**information content. The algorithm considers point source information, observation density, prior emissions, and**  
**country borders to construct an optimally reduced state vector (right panel) based on the user-specified number of**  
**state vector elements, maximum cluster size, and information content per element. The reduced state vector in the**  
360 **right panel has 600 elements with the number  $p$  of  $0.25^\circ \times 0.3125^\circ$  grid cells being aggregated ranging from  $p = 1$  (no**  
**aggregation) to  $p \approx 64$ . Methane plume map in the top left panel is from Carbon Mapper (Methane Dashboard |**  
**Carbon Mapper, 2024).**

Figure 3 illustrates our clustering algorithm with the example of the CONUS demo in Sect. 4. The user configures their  
desired number of state vector elements and maximum cluster size ( $2^\circ \times 2.5^\circ$  by default). The clustering algorithm first  
365 applies the IMI preview to estimate averaging kernel sensitivities,  $a_{ii}$ , (Eq. (4)), for each native resolution grid cell in the  
domain on the basis of the number of super-observations and the prior emission estimates. Cells that have an  $a_{ii}$  greater than  
a clustering threshold are kept at native resolution ( $p = 1$ ) in the state vector. They may also be kept at native resolution if  
flagged by the user or by a point source dataset (Sect. 3.2). The clustering threshold has a default value of the DOFS divided  
by the desired number of state vector elements but this can be configured by the user. The algorithm then performs a k-  
370 means clustering of proximate grid cell pairs ( $p = 2$ ) for the remaining lower-information grid cells on the basis of latitude,  
longitude, and  $a_{ii}$ , and retains pairs in the state vector that exceed the clustering threshold for the sum of their estimated  
averaging kernel sensitivities. The procedure is repeated for  $p = 3$ , and so on. The iteration stops when either the desired  
number of state vector elements is reached, the maximum cluster size is reached, or if continuing iteration would assign  
greater than the desired number of clusters. In the latter case, the remainder of the state vector is filled with elements of the  
375 maximum cluster size to achieve the desired number of state vector elements. At that point the final state vector is specified.

Users can determine a suitable number of state vector elements to balance information content and computational cost by  
running the IMI preview for varying state vector sizes and comparing the estimated DOFS (Fig. 4). The IMI preview



visualizes the clustered state vector and the gridded  $a_{ii}$  of each state vector element for user inspection. By adjusting the  
 380 clustering threshold and maximum cluster size with feedback from the IMI preview, users can effectively control the size  
 distribution of state vector elements. For example, in the CONUS inversion (Sect. 4) the estimated information content over  
 CONUS is bimodal, with many grid cells of relatively high information content and many with very low information  
 content. This bimodal distribution causes too many grid cell clusters to be above the default clustering threshold (estimated  
 DOFS/ $n$ ), leading to a premature filling of the grid with background clusters of the maximum cluster size to achieve a 600-  
 385 element state vector. If left unchecked, this would lead to low resolution background state vector elements having an  
 outsized sensitivity to the observations. To fix this issue we apply a clustering threshold of 2.0. Alternatively, the user could  
 increase the desired number of state vector elements, but the information content may not justify the added cost as illustrated  
 in Fig. 4 with the DOFS asymptote.



390 **Figure 4: Optimizing state vector size with the IMI preview (Sect. 2.2).** The DOFS are estimated from the IMI  
 preview for different user selections of state vector clustering sizes. Example is from the CONUS demo inversion  
 (Sect. 4), where the gain in information content levels off beyond 800 elements. We use 600 elements for purpose of  
 the demo.

### 3.7 Optimization of methane sink

395 IMI 1.0 only optimized methane emissions, but sinks also affect the methane concentrations. Global inversions commonly  
 optimize tropospheric OH (the main methane sink) in the state vector separately from emissions (Maasackers et al., 2019;  
 Yin et al., 2021). It is often argued that regional inversions do not need to optimize OH because the ventilation time scale is  
 much shorter than the methane lifetime (Sheng et al., 2018), but that argument is flawed because the exact same  
 consideration would apply to the effect of emissions. Tropospheric OH should be optimized in regional inversions if it



400 represents a major term in the regional methane budget relative to emissions, as is the case for tropical domains. In IMI 2.0 we provide the option to optimize the tropospheric OH concentration (as the methane loss frequency) averaged over the regional domain, or as hemispheric quantities for global inversions (Sect. 3.8), Prior estimates are the  $4^{\circ} \times 5^{\circ}$  global 3-D monthly fields of OH concentrations used in GEOS-Chem (Wecht et al., 2014). These fields yield a global methane lifetime of 10.7 years against tropospheric OH, within the observationally constrained range of  $11.2 \pm 1.3$  years from proxy  
405 observations (Prather et al., 2012). The default prior error standard deviation for the inversion is 10% (Y. Zhang et al., 2018) but can be modified by the user in the configuration file.

### 3.8 Global inversion capability

IMI 2.0 supports global inversions with optimization of methane emissions at up to  $2^{\circ} \times 2.5^{\circ}$  resolution as well as hemispheric OH concentrations (two additional state vector elements), following Qu et al. (2021). The same analytical  
410 inversion method used in regional inversions is applied globally. The global inversion is necessarily coarser than regional inversions and its purpose is to attribute global trends in methane concentrations within a consistent framework. The Kalman filter approach (Sect. 3.9) for time-dependent optimization of emissions can be used.

A critical requirement for global inversions is unbiased initial conditions. The smoothed TROPOMI archive described in  
415 Sect. 3.5 is effective for this purpose. It provides an unbiased synchronous representation of the stratosphere at the initial time that can then evolve with the forward simulation.

### 3.9 Temporal emission updates with Kalman filter

IMI 2.0 enables temporal emission updates and continuous emission monitoring at low latency with a Kalman filter approach as described by Varon et al. (2023). This workflow is depicted in Fig. 5. The IMI conducts successive methane inversions  
420 over user-specified time intervals (such as weekly or monthly), using observations for that interval. Prior emissions are taken as the posterior emissions of the preceding interval (Kalman filter), the original bottom-up estimates, or a combination of the two through a nudge factor  $\alpha$  ( $\alpha = 0$  for preceding interval,  $\alpha = 1$  for original bottom-up estimate). Relative error standard deviations on the prior emissions are not updated from their original values (50% in the default) because of unresolved prior error on the temporal variability of emissions. Varon et al. (2023) used  $\alpha = 0.1$  in their weekly inversions for the Permian  
425 Basin to retain some information from the original prior distribution and to prevent state vector elements from getting locked at low values when a fixed relative error on the prior emission is assumed. The state vector can be updated from one interval to the next with the adaptive k-means clustering scheme (Sect. 3.6) to take advantage of changing spatial patterns in information content. The latency of temporal emission updates is dependent on the availability of the IMI input data. At present the latency is about 1 month behind real time, limited by availability of the GEOS meteorological data to drive  
430 GEOS-Chem.



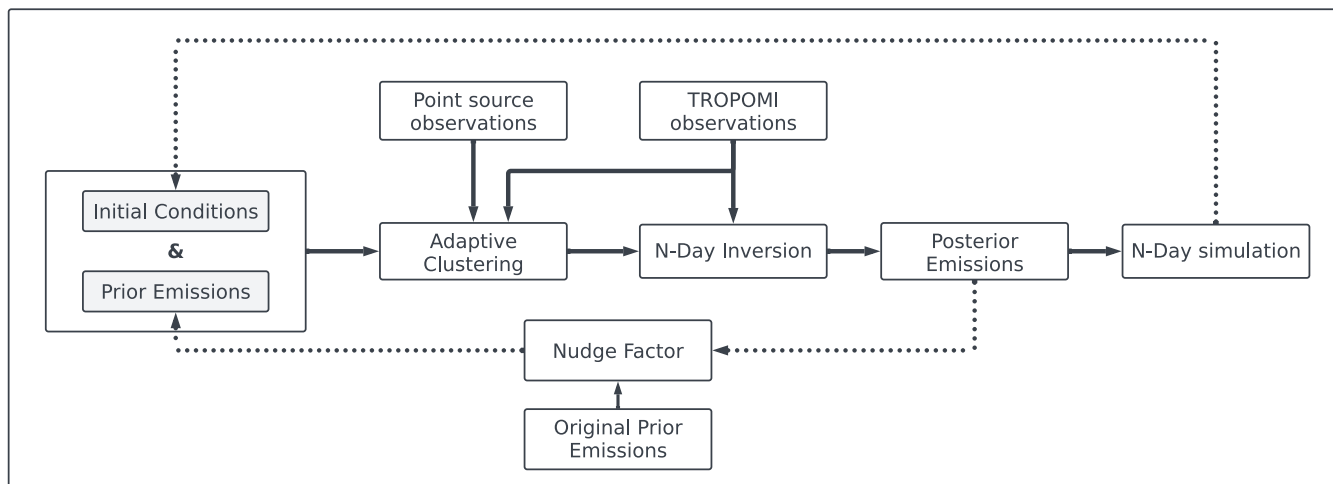


**Figure 5: Flowchart of the IMI 2.0 Kalman filter methodology for temporal emission updates with adaptive clustering enabled. Starting from initial conditions and bottom-up emission inventories used as prior estimates, the IMI reduces the state vector dimension by adaptive clustering (if desired) and conducts an inversion of TROPOMI observations for an N-day period to quantify the posterior emissions as averages for that period. At the end of the period, the posterior emissions are nudged back towards the original prior emissions (if desired) and used as prior estimates for the next N-day period.**

435

### 3.10 Updated bottom-up inventories as prior estimates

440 Table 3 lists the default bottom-up inventories used as prior estimates in IMI 2.0. Users may add or substitute their own prior estimates as NetCDF files to be read through HEMCO (Lin et al., 2021). New bottom-up inventories introduced in IMI 2.0 include worldwide emissions from hydroelectric reservoirs (Delwiche et al., 2022), an updated gridded version of US emissions from the EPA Greenhouse Gas Inventory (Maasackers et al., 2023), and updated global anthropogenic emissions from EDGAR v8 (Crippa et al., 2023). Bottom-up anthropogenic inventories are reported with lag times of a few years or more and we use as default the most recent reported year, but this is of little consequence because most reported anthropogenic emissions and their distributions generally vary little from year to year. Wetland emissions can have large year-to-year variability but also large uncertainties, so we use as default the monthly emissions from the mean of the WetCHARTs inventory ensemble for individual years (Bloom et al., 2021), which users can replace by monthly WetCHARTs or LPJ-wsl climatologies. GFED4 open fire emissions have daily temporal resolution and are for individual years.

450

455



**Table 3: Default prior emission inventories in IMI 2.0**

<b>Anthropogenic</b>	
United States	EPA Gridded GHGI v2 – Express Extension (Maasakkers et al., 2023)
Mexico	INECC (Scarpelli et al., 2020)
Canada	ECCC NIR (Scarpelli et al., 2022a)
Rest of world	
- Fuel Exploitation	GFEI v2.0 (Scarpelli et al., 2022b)
- Other	EDGAR v8 (Crippa et al., 2023)
Hydroelectric reservoirs	ResME (Delwiche et al., 2022)
<b>Natural</b>	
Wetlands <sup>a</sup>	WetCHARTs v1.3.1 (Bloom et al., 2021); LPJ-wsl (Z. Zhang et al., 2016)
Geological seeps	Etiopie et al. (2019) scaled to 2 Tg a <sup>-1</sup> (Hmiel et al., 2020)
Open fires	GFED4 (Randerson et al., 2017)
Termites	Fung et al. (1991)

<sup>a</sup> The IMI uses as default monthly wetland emissions from the mean of the WetCHARTs ensemble, but users can replace this default with WetCHARTs or LPJ-wsl climatologies.

### 3.11 Lognormal error PDFs for heavy tailed emissions

460 IMI 2.0 includes an option to use lognormal error PDFs for the prior emission estimates. Methane emission distributions often exhibit heavy tails towards higher values in areas with highly variable sources, which can be better characterized using lognormal errors rather than normal errors (Yuan et al., 2015; Cui et al., 2019; Maasakkers et al., 2019; Chen et al., 2023). An added benefit of using lognormal errors is that it enforces positivity in the posterior solution. Solving the inversion in log space is nonlinear, requiring an iterative approach to find the solution through repeated update of the Jacobian matrix **K** (Rodgers, 2000). Updates to **K** in log space are readily computed through simple scaling without having to re-run GEOS-Chem (Maasakkers et al., 2019). The iterative nature of the solution does not significantly increase computational cost because the matrix operations are fast. Only the prior emission elements of the state vector in the region of interest are optimized in log space; buffer elements, boundary conditions, and OH concentrations continue to be optimized with normal errors (Maasakkers et al., 2019; Chen et al., 2022).

470

When using the lognormal error PDFs option, the inversion optimizes the median of the posterior PDF, starting from the median of the prior PDF. But the prior estimates reported in Table 3 should be viewed as the means of their PDFs, with a geometric error standard deviation  $\sigma_g$  (for example,  $\sigma_g = 2$  states a factor of 2 uncertainty). The median of a lognormal PDF is related to its mean by  $\mathbf{x}_{median} = \mathbf{x}_{mean} \exp [-(\ln \sigma_g^2)/2]$  and we apply this correction to the prior estimates for input to the inversion. The inversion then returns the median of the posterior PDF with posterior error covariance matrix in log space.

475



We convert the median to the mean of the posterior PDF with geometric error standard deviations by following the reverse of the above procedure. See Hancock et al. (2024) for further details on the method.

### 3.12 Enriched output

IMI 1.0 output included gridded posterior emission estimates with error standard deviations, averaging kernel sensitivities, and tables of emission totals. It also compared the GEOS-Chem simulations with posterior versus prior emissions to the TROPOMI observations as diagnostic of the improved fit resulting from the inversion, with means and spatial standard deviations of the time-averaged GEOS-Chem – TROPOMI differences as indicators. Here we add tabulated and gridded posterior emissions by source sectors, using the prior sectoral contributions within individual grid cells to assign corrections from the inversion to individual sectors (Wecht et al., 2014). The sectoral output can be further partitioned by individual countries within the inversion domain. We also provide timeseries of emissions when using temporal emission updates (Sect. 3.9). Output for the IMI preview now includes gridded visualization of both TROPOMI datasets (operational and blended), overlay of point source locations (Sect. 3.2) on the map of prior emissions, and visualization of estimated averaging kernel sensitivities. The averaging kernel sensitivities are estimated in the preview using the density of super-observations (Sect 3.4) with a modified version of the IMI 1.0 formula in Eq. (4):

490

$$a_{ii} = \frac{\sigma_{a_i}^2}{\sigma_{a_i}^2 + \frac{(\sigma_{super,i}/k)^2}{m_{super,i}}}, \quad (6)$$

where the variables are the same as in Eq. (4) except  $\sigma_{super,i}$  and  $m_{super,i}$ .  $\sigma_{super,i}$  is the observational error standard deviation for state vector element  $i$  calculated as in Eq. (5) using the average number of grid cell observations,  $P$ , within that element over the inversion time period.  $m_{super,i}$  is the number of super-observations for state vector element  $i$  over the inversion time period. The IMI configuration file is also written to the output directory for user reference.

### 495 3.13 IMI Docker container

IMI 2.0 includes a software container to facilitate installation of the IMI to local systems and support scheduled inversion workflows (e.g., once a week or once a month). A container is a lightweight, standalone, and executable software package that encapsulates an application and all its dependencies, including libraries, frameworks, and system tools. Creating an IMI container provides a stable and reproducible environment. It ensures that the IMI can run consistently across different systems, such as local clusters, cloud servers, and even local computers regardless of operating system. Once the container is downloaded, the only dependency needed to run the software is Docker® (a container engine). The necessary input data is automatically downloaded from the AWS cloud upon running the IMI container.

500



505 The IMI container is built in two stages: a base container and an operational container. The base container builds the environment and dependencies needed to run the IMI (python packages, forward model dependencies, system tools). The build of the base environment is performed with two commonly used scientific package managers, Spack™ and Micromamba™. The operational container build simply downloads and configures the IMI source code into the container. The operational container is built automatically via GitHub Actions upon new IMI version releases and archived on a publicly accessible cloud repository with download instructions on the IMI documentation site.

510

An application of the containerized IMI is to support the US GHG Center, a multi-agency initiative to provide a trusted repository of greenhouse gas data from models and observations on the AWS cloud (U.S. Greenhouse Gas Center, 2024). The US GHG Center uses a Multi-Mission Algorithm and Analysis Platform (MAAP; Earthdata, 2024) cloud environment designed to ingest containers. The IMI operates within MAAP to provide an inversion tool as part of the US GHG Center capabilities.

515

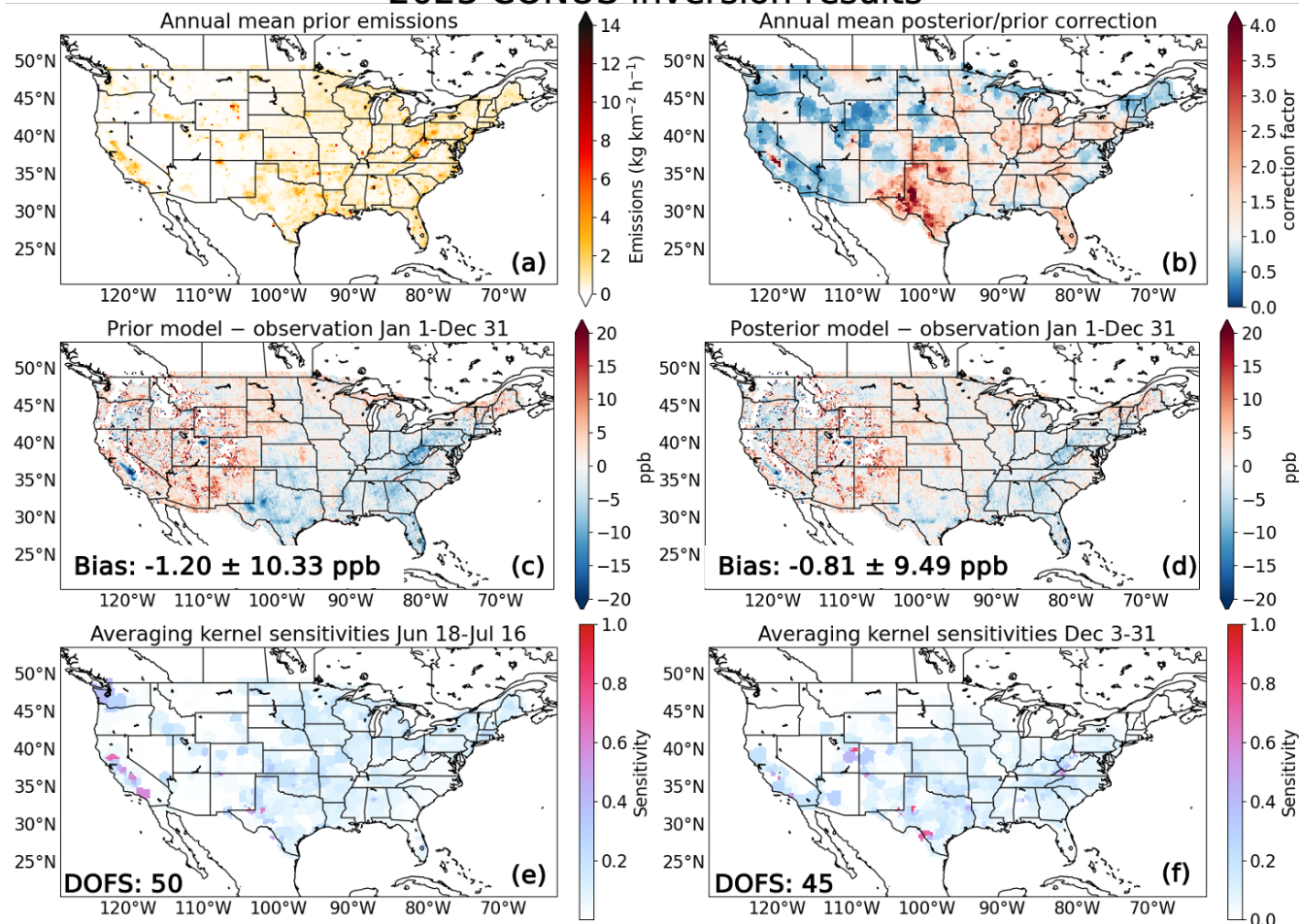
#### 4 Example application to the contiguous United States

To demonstrate the new capabilities of the IMI, we show an example out-of-the-box application of IMI 2.0 to quantify methane emissions in the contiguous United States (CONUS). The inversion period runs from January 1, 2023 to December 31, 2023 with 28-day Kalman filter emission updates and the blended TROPOMI+GOSAT observations. The prior emissions are the defaults described in Sect. 3.10. The Kalman filter is designed to resolve any seasonal variation not included or wrongly included in the prior estimates (Table 3). The CONUS domain is provided as a shapefile, and Canada and Mexico are included as 16 buffer clusters. The inversion uses GEOS-Chem at  $0.25^\circ \times 0.3125^\circ$  resolution which is therefore the native resolution of the state vector, corresponding to 11,698 elements over CONUS. We apply adaptive state vector clustering to reduce the state vector size from 11,698 to 600 elements for each 28-day inversion interval, as described in Sect. 3.9 and illustrated in Fig. 3. We apply a clustering threshold of 2.0 to prevent a bimodal size distribution in elements with high information content, as described in Sect. 3.6. We apply a regularization parameter  $\gamma = 0.2$  to prevent overfit. The optimal value of  $\gamma$  was determined such that  $(\hat{\mathbf{x}} - \mathbf{x}_A)^T \mathbf{S}_A^{-1} (\hat{\mathbf{x}} - \mathbf{x}_A) \approx n \pm \sqrt{2n}$  following Lu et al. (2021), corresponding to the expected value of the chi-square distribution. Other configuration settings for this demo CONUS inversion are given in Table 2.

530



## 2023 CONUS inversion results



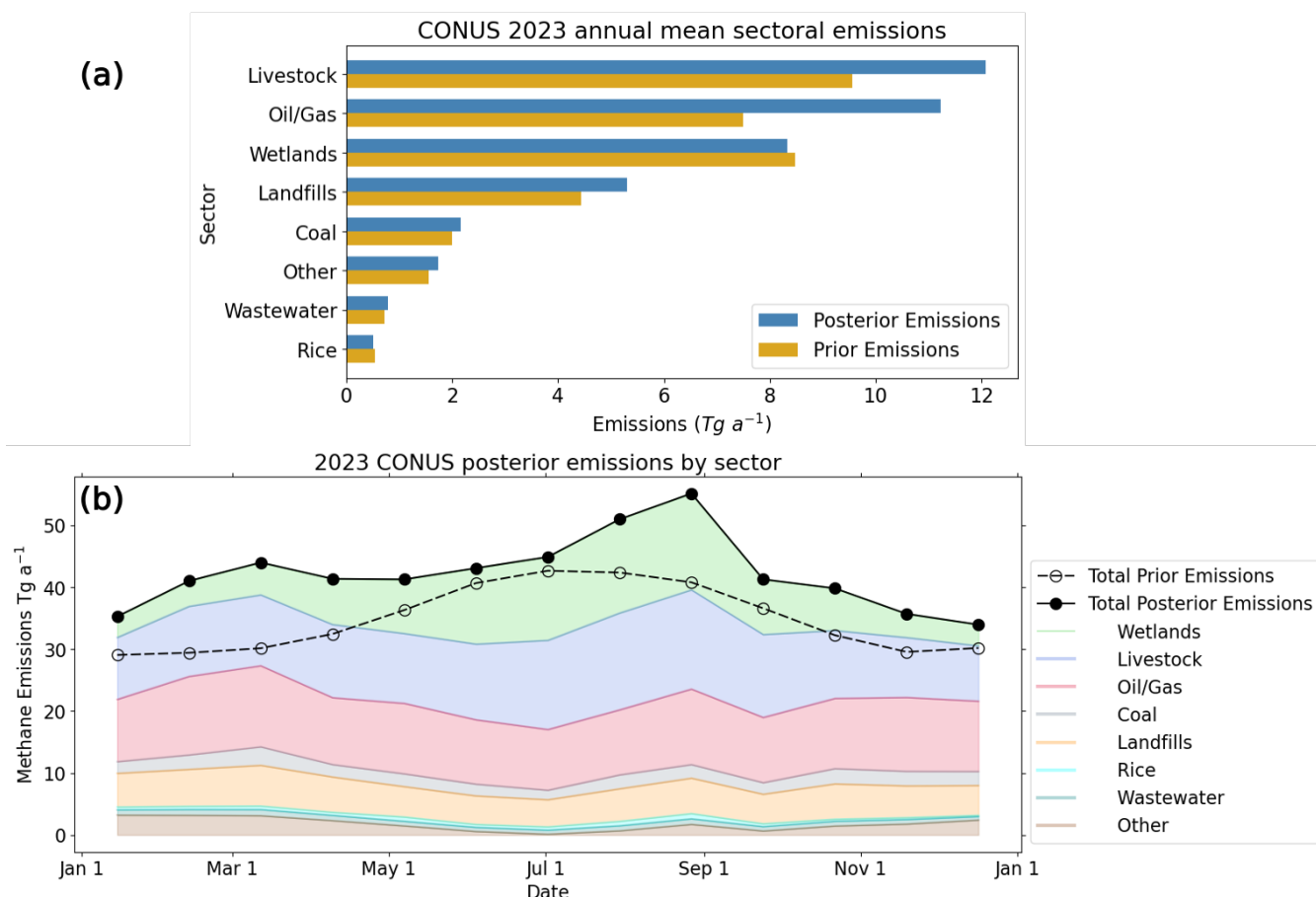
535 Figure 6: Application of IMI 2.0 to a demo CONUS inversion with configuration settings given in Table 2. The  
inversion is for 1 year (January 1 – December 31, 2023) over the CONUS domain provided as a shapefile and with  
buffer clusters for Canada and Mexico. Observations are from the blended TROPOMI+GOSAT product (Balasus et  
al., 2023). The top row shows the annual average prior emissions (a) and correction factors from the inversion (b).  
The middle row shows the differences in ppb between the observations and simulated concentrations using the  
original prior emissions (c) and the posterior emissions (d) for each inversion interval. Mean bias and spatial  
standard deviations are given inset. The bottom row shows the averaging kernel sensitivities for the June 18 – July 16  
540 (e) and December 3 – 30 (f) inversion intervals with DOFS inset.

Figure 6 shows the spatial distribution of results as returned by the IMI. Starting from the EPA Gridded GHGI v2 – Express  
Extension Greenhouse Gas Inventory taken as prior estimate on January 1, 2023, together with other prior estimates (Table  
3), the inversion applies mean correction factors for each 28-day period resulting in annual mean correction factors shown in  
Figure 6. A GEOS-Chem simulation with these posterior emission estimates provides a better fit to the TROPOMI data over  
545 the inversion domain than with the prior estimates, as indicated by the monthly mean bias and spatial standard deviation of



the  $\Delta(\text{GEOS-Chem} - \text{TROPOMI})$  difference. The averaging kernel sensitivities returned by the inversion are highest, approaching unity, in regions of high emissions, and near zero in regions of low emissions. They are generally higher in summer than winter for northern CONUS because of a higher fraction of successful TROPOMI retrievals.

550 Figure 7 shows the time series of CONUS 28-day emissions and the mean annual totals by sector. The annual mean prior emission is 34 Tg a<sup>-1</sup> and peaks in July. We find an annual mean posterior emission of 42 Tg a<sup>-1</sup> for 2023 with mean DOFS per 28-day inversion interval of 49 and maximum emission in September. The seasonal offset from July to September is largely driven by wetlands, which may be explained by WetCHARTs' use of air temperature rather than soil temperature to predict wetlands emissions. The same issue is found for boreal wetlands (East et al., 2024). Upward corrections to emissions  
 555 are largest for livestock and oil/gas, as is apparent in the posterior/prior correction patterns in Figure 6. Our results are broadly in agreement with the range of emission estimates for other CONUS inverse studies (Lu et al., 2022, 2023; Worden et al., 2022; Shen et al., 2023; Nesser et al., 2024). Differences could be investigated in the IMI with sensitivity inversions swapping prior emissions, observational products, and inversion parameters.





565 **Figure 7: CONUS sectoral emissions for 2023 and 28-day variability as obtained by the demo inversion using IMI 2.0. (a) Compares annual mean posterior and prior 2023 emission estimates by sector. (b) Shows the evolution of sectoral emissions over 28-day inversion intervals. Total prior emissions are shown by the dotted black line. Total posterior emissions shown by solid black line. Each symbol on the prior/posterior emissions line represents the middle of the 28-day inversion interval.**

## 5 Conclusions and future work

The Integrated Methane Inversion (IMI) is a cloud-based, user-friendly software tool for researchers and stakeholders to infer methane emissions from TROPOMI satellite observations. Here we presented major new developments in IMI 2.0 that increase its value and reliability to quantify emissions from the global scale down to 25-km resolution, incorporating also  
570 additional information from point source imaging satellite instruments. IMI 2.0 features a capability for low-latency monitoring of the temporal variability of emissions for any user-selected region. It can be used on the cloud or downloaded to local compute clusters. Full documentation and a user's manual are available at <https://imi.readthedocs.io>.

The IMI is a living software tool with a steady stream of development from scientific users. We have already launched new  
575 developments to include: (1) reducing latency to 2-3 days; (2) increasing the spatial resolution to 12×12 km<sup>2</sup>; (3) integrating methane observations from new satellite instruments (MethaneSAT); (4) incorporating information from point source imagers (GHGSat, Carbon Mapper) directly into the inversion; (5) adding an IMI preview tool to provide guidance on boundary conditions; (6) extending the IMI to CO<sub>2</sub>. These and other developments will provide the basis for IMI 3.0.

### 580 *Code availability*

The IMI source code and documentation is available at <https://imi.seas.harvard.edu/>. The code used in this paper is permanently archived at <https://zenodo.org/doi/10.5281/zenodo.6081933>.

### *Data availability*

585 The TROPOMI methane data are available on the Amazon Web Services (AWS) cloud at <https://registry.opendata.aws/sentinel5p/> (last access: 26 April 2024; AWS, 2024). The blended TROPOMI+GOSAT data are available at <https://registry.opendata.aws/blended-tropomi-gosat-methane/> (Balasus et al., 2023). The GEOS-FP emission fields, boundary condition fields, and meteorological fields are available on AWS at <https://registry.opendata.aws/geoschem-input-data/> (last access: 25 April 2024; AWS, 2024).

590

### *Author contributions*

LAE, DJV, MS, and DJJ contributed to the study design. LAE, DJV, MS, NB, SHE, MH, AOO, and JDE developed the model code. LAE, DJJ, DJV, NB, HN, and ZC contributed to the development of methods. LAE performed the analysis and wrote the original draft. All authors reviewed and edited the manuscript.



595

### *Competing interests*

The contact author has declared that none of the authors has any competing interests.

### *Acknowledgments*

600 This work was funded by ExxonMobil Technology and Engineering Company, by the Harvard Initiative on Reducing Global Methane Emissions, the NASA Carbon Monitoring System, and by the NASA Jet Propulsion Laboratory initiative for the US GHG Center. Part of this research was carried out at the Jet Propulsion Laboratory, California Institute of Technology, under a contract with the National Aeronautics and Space Administration. This research was supported in part by an appointment to the NASA Postdoctoral Program at the Jet Propulsion Laboratory, California Institute of Technology  
605 administered by Oak Ridge Associated Universities under contract with NASA.

### **References**

- 610 Balasus, N., Jacob, D. J., Lorente, A., Maasackers, J. D., Parker, R. J., Boesch, H., Chen, Z., Kelp, M. M., Nesser, H., and Varon, D. J.: A blended TROPOMI+GOSAT satellite data product for atmospheric methane using machine learning to correct retrieval biases, *Atmos. Meas. Tech.*, 16, 3787–3807, <https://doi.org/10.5194/amt-16-3787-2023>, 2023.
- Baray, S., Vogel, F. R., Varon, D. J., Estrada, L., Balasus, N., Jones, D. B., McLinden, C. A., Griffin, D., Duren, R., and Cusworth, D.: Monitoring methane emissions in Western Canada from space using a constellation of satellites: TROPOMI, GOSAT-1/2, GHGSat, and Carbon Mapper, Presented at the American Geophysical Union 2023 Conference, Retrieved from <https://agu.confex.com/agu/fm23/meetingapp.cgi/Paper/1415398>, 2023.
- 615 Berchet, A., Sollum, E., Thompson, R. L., Pison, I., Thanwerdas, J., Broquet, G., Chevallier, F., Aalto, T., Berchet, A., Bergamaschi, P., Brunner, D., Engelen, R., Fortems-Cheiney, A., Gerbig, C., Groot Zwaaftink, C. D., Haussaire, J.-M., Henne, S., Houweling, S., Karstens, U., Kutsch, W. L., Luijkx, I. T., Monteil, G., Palmer, P. I., van Peet, J. C. A., Peters, W., Peylin, P., Potier, E., Rödenbeck, C., Saunio, M., Scholze, M., Tsuruta, A., and Zhao, Y.: The Community Inversion Framework v1.0: a unified system for atmospheric inversion studies, *Geoscientific Model Development*, 14, 5331–5354,  
620 <https://doi.org/10.5194/gmd-14-5331-2021>, 2021.
- Bey, I., Jacob, D. J., Yantosca, R. M., Logan, J. A., Field, B. D., Fiore, A. M., Li, Q., Liu, H. Y., Mickley, L. J., and Schultz, M. G.: Global modeling of tropospheric chemistry with assimilated meteorology: Model description and evaluation, *Journal of Geophysical Research: Atmospheres*, 106, 23073–23095, <https://doi.org/10.1029/2001JD000807>, 2001.
- Bloom, A. A., Bowman, K. W., Lee, M., Turner, A. J., Schroeder, R., Worden, J. R., Weidner, R. J., McDonald, K. C., and  
625 Jacob, D. J.: CMS: Global 0.5-deg Wetland Methane Emissions and Uncertainty (WetCHARTs v1.3.1), ORNL DAAC, <https://doi.org/10.3334/ORNLDAAC/1915>, 2021.
- Brasseur, G. P. and Jacob, D. J.: *Modeling of Atmospheric Chemistry*, Cambridge University Press, Cambridge, <https://doi.org/10.1017/9781316544754>, 2017.
- Carbon Mapper Dashboard:  
630 [https://data.carbonmapper.org/?gasType=CH4&emission\\_min=3600&details=CH4\\_1B2\\_250m\\_-101.46240\\_31.44581%3Fstatus%3Dnot\\_deleted#14.98/31.44096/-101.45689](https://data.carbonmapper.org/?gasType=CH4&emission_min=3600&details=CH4_1B2_250m_-101.46240_31.44581%3Fstatus%3Dnot_deleted#14.98/31.44096/-101.45689), last access: 19 May 2024.





- Cardoso-Saldaña, F. J. and Allen, D. T.: Projecting the Temporal Evolution of Methane Emissions from Oil and Gas Production Sites, *Environ. Sci. Technol.*, 54, 14172–14181, <https://doi.org/10.1021/acs.est.0c03049>, 2020.
- 635 Chabrillat, S., Vigouroux, C., Christophe, Y., Engel, A., Errera, Q., Minganti, D., Monge-Sanz, B. M., Segers, A., and Mahieu, E.: Comparison of mean age of air in five reanalyses using the BASCOE transport model, *Atmospheric Chemistry and Physics*, 18, 14715–14735, <https://doi.org/10.5194/acp-18-14715-2018>, 2018.
- Chen, Z., Jacob, D. J., Nesser, H., Sulprizio, M. P., Lorente, A., Varon, D. J., Lu, X., Shen, L., Qu, Z., Penn, E., and Yu, X.: Methane emissions from China: a high-resolution inversion of TROPOMI satellite observations, *Atmospheric Chemistry and Physics*, 22, 10809–10826, <https://doi.org/10.5194/acp-22-10809-2022>, 2022.
- 640 Chen, Z., Jacob, D. J., Gautam, R., Omara, M., Stavins, R. N., Stowe, R. C., Nesser, H., Sulprizio, M. P., Lorente, A., Varon, D. J., Lu, X., Shen, L., Qu, Z., Pendergrass, D. C., and Hancock, S.: Satellite quantification of methane emissions and oil-gas methane intensities from individual countries in the Middle East and North Africa: implications for climate action, *Atmospheric Chemistry and Physics*, 23, 5945–5967, <https://doi.org/10.5194/acp-23-5945-2023>, 2023.
- 645 Crippa, M., Guizzardi, D., Pagani, F., Schiavina, M., Melchiorri, M., Pisoni, E., Graziosi, F., Muntean, M., Maes, J., Dijkstra, L., Van Damme, M., Clarisse, L., and Coheur, P.: Insights on the spatial distribution of global, national and sub-national GHG emissions in EDGARv8.0, *Earth System Science Data Discussions*, 1–28, <https://doi.org/10.5194/essd-2023-514>, 2023.
- 650 Cui, Y. Y., Henze, D. K., Brioude, J., Angevine, W. M., Liu, Z., Bousserez, N., Guerrette, J., McKeen, S. A., Peischl, J., Yuan, B., Ryerson, T., Frost, G., and Trainer, M.: Inversion Estimates of Lognormally Distributed Methane Emission Rates From the Haynesville-Bossier Oil and Gas Production Region Using Airborne Measurements, *Journal of Geophysical Research: Atmospheres*, 124, 3520–3531, <https://doi.org/10.1029/2018JD029489>, 2019.
- Cusworth, D. H., Duren, R. M., Yadav, V., Thorpe, A. K., Verhulst, K., Sander, S., Hopkins, F., Rafiq, T., and Miller, C. E.: Synthesis of Methane Observations Across Scales: Strategies for Deploying a Multitiered Observing Network, *Geophysical Research Letters*, 47, e2020GL087869, <https://doi.org/10.1029/2020GL087869>, 2020.
- 655 Cusworth, D. H., Duren, R. M., Ayasse, A. K., Jiorle, R., Howell, K., Aubrey, A., Green, R. O., Eastwood, M. L., Chapman, J. W., Thorpe, A. K., Heckler, J., Asner, G. P., Smith, M. L., Thoma, E., Krause, M. J., Heins, D., and Thorneloe, S.: Quantifying methane emissions from United States landfills, *Science*, 383, 1499–1504, <https://doi.org/10.1126/science.adi7735>, 2024.
- 660 Delwiche, K. B., Harrison, J. A., Maasackers, J. D., Sulprizio, M. P., Worden, J., Jacob, D. J., and Sunderland, E. M.: Estimating Drivers and Pathways for Hydroelectric Reservoir Methane Emissions Using a New Mechanistic Model, *Journal of Geophysical Research: Biogeosciences*, 127, e2022JG006908, <https://doi.org/10.1029/2022JG006908>, 2022.
- East, J. D., Jacob, D. J., Balasus, N., Bloom, A. A., Bruhwiler, L., Chen, Z., Kaplan, J. O., Mickley, L. J., Mooring, T. A., Penn, E., Poulter, B., Sulprizio, M. P., Worden, J. R., Yantosca, R. M., and Zhang, Z.: Interpreting the Seasonality of Atmospheric Methane, *Geophysical Research Letters*, 51, e2024GL108494, <https://doi.org/10.1029/2024GL108494>, 2024.
- 665 Etiopie, G., Ciotoli, G., Schwietzke, S., and Schoell, M.: Gridded maps of geological methane emissions and their isotopic signature, *Earth System Science Data*, 11, 1–22, <https://doi.org/10.5194/essd-11-1-2019>, 2019.
- 670 Forster, P., Storelvmo, T., Armour, K., Collins, W., Dufresne, J.-L., Frame, D., Lunt, D. J., Mauritsen, T., Palmer, M. D., Watanabe, M., Wild, M., and Zhang, H.: The Earth’s Energy Budget, Climate Feedbacks and Climate Sensitivity, in: *Climate Change 2021 – The Physical Science Basis: Working Group I Contribution to the Sixth Assessment Report of the Intergovernmental Panel on Climate Change*, Cambridge University Press, 923–1054, 2021.



Fung, I., John, J., Lerner, J., Matthews, E., Prather, M., Steele, L. P., and Fraser, P. J.: Three-dimensional model synthesis of the global methane cycle, *Journal of Geophysical Research: Atmospheres*, 96, 13033–13065, <https://doi.org/10.1029/91JD01247>, 1991.

Global Methane Pledge: <https://www.globalmethanepledge.org/>, last access: 25 September 2023.

675 Hancock, S. E., Jacob, D., Chen, Z., Nesser, H., Davitt, A., Varon, D. J., Sulprizio, M. P., Balasus, N., Estrada, L. A., East, J. D., Penn, E., Randles, C. A., Worden, J., Aben, I., Parker, R. J., and Maasakkers, J. D.: Satellite quantification of methane emissions from South American countries: A high-resolution inversion of TROPOMI and GOSAT observations, *EGUsphere*, 1–33, <https://doi.org/10.5194/egusphere-2024-1763>, 2024.

680 Heald, C. L., Jacob, D. J., Jones, D. B. A., Palmer, P. I., Logan, J. A., Streets, D. G., Sachse, G. W., Gille, J. C., Hoffman, R. N., and Nehr Korn, T.: Comparative inverse analysis of satellite (MOPITT) and aircraft (TRACE-P) observations to estimate Asian sources of carbon monoxide, *Journal of Geophysical Research: Atmospheres*, 109, <https://doi.org/10.1029/2004JD005185>, 2004.

685 Hemati, M., Mahdianpari, M., Nassar, R., Shiri, H., and Mohammadimanesh, F.: Urban methane emission monitoring across North America using TROPOMI data: an analytical inversion approach, *Sci Rep*, 14, 9041, <https://doi.org/10.1038/s41598-024-58995-8>, 2024.

Hmiel, B., Petrenko, V. V., Dyonisius, M. N., Buizert, C., Smith, A. M., Place, P. F., Harth, C., Beaudette, R., Hua, Q., Yang, B., Vimont, I., Michel, S. E., Severinghaus, J. P., Etheridge, D., Bromley, T., Schmitt, J., Faïn, X., Weiss, R. F., and Dlugokencky, E.: Preindustrial 14CH<sub>4</sub> indicates greater anthropogenic fossil CH<sub>4</sub> emissions, *Nature*, 578, 409–412, <https://doi.org/10.1038/s41586-020-1991-8>, 2020.

690 International Methane Emissions Observatory: <http://www.unep.org/topics/energy/methane/international-methane-emissions-observatory>, last access: 1 May 2024.

Jacob, D. J., Turner, A. J., Maasakkers, J. D., Sheng, J., Sun, K., Liu, X., Chance, K., Aben, I., McKeever, J., and Frankenberg, C.: Satellite observations of atmospheric methane and their value for quantifying methane emissions, *Atmospheric Chemistry and Physics*, 16, 14371–14396, <https://doi.org/10.5194/acp-16-14371-2016>, 2016.

695 Jacob, D. J., Varon, D. J., Cusworth, D. H., Dennison, P. E., Frankenberg, C., Gautam, R., Guanter, L., Kelley, J., McKeever, J., Ott, L. E., Poulter, B., Qu, Z., Thorpe, A. K., Worden, J. R., and Duren, R. M.: Quantifying methane emissions from the global scale down to point sources using satellite observations of atmospheric methane, *Atmospheric Chemistry and Physics*, 22, 9617–9646, <https://doi.org/10.5194/acp-22-9617-2022>, 2022.

700 Li, S., Wang, C., Gao, P., Zhao, B., Jin, C., Zhao, L., He, B., and Xue, Y.: High-Spatial-Resolution Methane Emissions Calculation Using TROPOMI Data by a Divergence Method, *Atmosphere*, 14, 388, <https://doi.org/10.3390/atmos14020388>, 2023.

705 Lin, H., Jacob, D. J., Lundgren, E. W., Sulprizio, M. P., Keller, C. A., Fritz, T. M., Eastham, S. D., Emmons, L. K., Campbell, P. C., Baker, B., Saylor, R. D., and Montuoro, R.: Harmonized Emissions Component (HEMCO) 3.0 as a versatile emissions component for atmospheric models: application in the GEOS-Chem, NASA GEOS, WRF-GC, CESM2, NOAA GEFS-Aerosol, and NOAA UFS models, *Geoscientific Model Development*, 14, 5487–5506, <https://doi.org/10.5194/gmd-14-5487-2021>, 2021.

Lin, S.-J. and Rood, R. B.: *Multidimensional Flux-Form Semi-Lagrangian Transport Schemes*, 1996.



- 710 Lorente, A., Borsdorff, T., Butz, A., Hasekamp, O., aan de Brugh, J., Schneider, A., Wu, L., Hase, F., Kivi, R., Wunch, D., Pollard, D. F., Shiomi, K., Deutscher, N. M., Velazco, V. A., Roehl, C. M., Wennberg, P. O., Warneke, T., and Landgraf, J.: Methane retrieved from TROPOMI: improvement of the data product and validation of the first 2 years of measurements, *Atmospheric Measurement Techniques*, 14, 665–684, <https://doi.org/10.5194/amt-14-665-2021>, 2021.
- Lorente, A., Borsdorff, T., Martinez-Velarte, M. C., and Landgraf, J.: Accounting for surface reflectance spectral features in TROPOMI methane retrievals, *Atmospheric Measurement Techniques*, 16, 1597–1608, <https://doi.org/10.5194/amt-16-1597-2023>, 2023.
- 715 Lu, X., Jacob, D. J., Zhang, Y., Maasackers, J. D., Sulprizio, M. P., Shen, L., Qu, Z., Scarpelli, T. R., Nesser, H., Yantosca, R. M., Sheng, J., Andrews, A., Parker, R. J., Boesch, H., Bloom, A. A., and Ma, S.: Global methane budget and trend, 2010–2017: complementarity of inverse analyses using in situ (GLOBALVIEWplus CH<sub>4</sub> ObsPack) and satellite (GOSAT) observations, *Atmospheric Chemistry and Physics*, 21, 4637–4657, <https://doi.org/10.5194/acp-21-4637-2021>, 2021.
- 720 Lu, X., Jacob, D. J., Wang, H., Maasackers, J. D., Zhang, Y., Scarpelli, T. R., Shen, L., Qu, Z., Sulprizio, M. P., Nesser, H., Bloom, A. A., Ma, S., Worden, J. R., Fan, S., Parker, R. J., Boesch, H., Gautam, R., Gordon, D., Moran, M. D., Reuland, F., Villasana, C. A. O., and Andrews, A.: Methane emissions in the United States, Canada, and Mexico: evaluation of national methane emission inventories and 2010–2017 sectoral trends by inverse analysis of in situ (GLOBALVIEWplus CH<sub>4</sub> ObsPack) and satellite (GOSAT) atmospheric observations, *Atmospheric Chemistry and Physics*, 22, 395–418, <https://doi.org/10.5194/acp-22-395-2022>, 2022.
- 725 Lu, X., Jacob, D. J., Zhang, Y., Shen, L., Sulprizio, M. P., Maasackers, J. D., Varon, D. J., Qu, Z., Chen, Z., Hmiel, B., Parker, R. J., Boesch, H., Wang, H., He, C., and Fan, S.: Observation-derived 2010–2019 trends in methane emissions and intensities from US oil and gas fields tied to activity metrics, *Proceedings of the National Academy of Sciences*, 120, e2217900120, <https://doi.org/10.1073/pnas.2217900120>, 2023.
- 730 Maasackers, J. D., Jacob, D. J., Sulprizio, M. P., Scarpelli, T. R., Nesser, H., Sheng, J.-X., Zhang, Y., Hersher, M., Bloom, A. A., Bowman, K. W., Worden, J. R., Janssens-Maenhout, G., and Parker, R. J.: Global distribution of methane emissions, emission trends, and OH concentrations and trends inferred from an inversion of GOSAT satellite data for 2010–2015, *Atmospheric Chemistry and Physics*, 19, 7859–7881, <https://doi.org/10.5194/acp-19-7859-2019>, 2019.
- 735 Maasackers, J. D., McDuffie, E. E., Sulprizio, M. P., Chen, C., Schultz, M., Brunelle, L., Thrush, R., Steller, J., Sherry, C., Jacob, D. J., Jeong, S., Irving, B., and Weitz, M.: A Gridded Inventory of Annual 2012–2018 U.S. Anthropogenic Methane Emissions, *Environ. Sci. Technol.*, 57, 16276–16288, <https://doi.org/10.1021/acs.est.3c05138>, 2023.
- McNorton, J., Bousserez, N., Agustí-Panareda, A., Balsamo, G., Cantarello, L., Engelen, R., Huijnen, V., Inness, A., Kipling, Z., Parrington, M., and Ribas, R.: Quantification of methane emissions from hotspots and during COVID-19 using a global atmospheric inversion, *Atmospheric Chemistry and Physics*, 22, 5961–5981, <https://doi.org/10.5194/acp-22-5961-2022>, 2022.
- 740 Methane Plume Maps: <https://earth.sron.nl/methane-emissions/>, last access: 18 May 2024.
- Mooring, T. A., Jacob, D. J., Sulprizio, M. P., Balasus, N., Baier, B. C., Kiefer, M., Murray, L. T., Yantosca, R. M., East, J. D., Bruhwiler, L. M. P., and Andrews, A.: Evaluating Stratospheric Methane in GEOS-Chem with Satellite and Balloon Observations, Presented at the American Meteorological Society 104<sup>th</sup> Annual Meeting, Retrieved from <https://ams.confex.com/ams/104ANNUAL/meetingapp.cgi/Paper/437083>, 2024.
- 745 Multi-Mission Algorithm and Analysis Platform (MAAP) | Earthdata: <https://www.earthdata.nasa.gov/esds/maap>, last access: 2 May 2024.



- Murray, L. T.: Lightning NO<sub>x</sub> and Impacts on Air Quality, *Curr Pollution Rep*, 2, 115–133, <https://doi.org/10.1007/s40726-016-0031-7>, 2016.
- 750 Naik, V., Voulgarakis, A., Fiore, A. M., Horowitz, L. W., Lamarque, J.-F., Lin, M., Prather, M. J., Young, P. J., Bergmann, D., Cameron-Smith, P. J., Cionni, I., Collins, W. J., Dalsøren, S. B., Doherty, R., Eyring, V., Faluvegi, G., Folberth, G. A., Josse, B., Lee, Y. H., MacKenzie, I. A., Nagashima, T., van Noije, T. P. C., Plummer, D. A., Righi, M., Rumbold, S. T., Skeie, R., Shindell, D. T., Stevenson, D. S., Strode, S., Sudo, K., Szopa, S., and Zeng, G.: Preindustrial to present-day changes in tropospheric hydroxyl radical and methane lifetime from the Atmospheric Chemistry and Climate Model Intercomparison Project (ACCMIP), *Atmospheric Chemistry and Physics*, 13, 5277–5298, <https://doi.org/10.5194/acp-13-5277-2013>, 2013.
- 755 Nathan, B., Maasakkers, J. D., Naus, S., Gautam, R., Omara, M., Varon, D. J., Sulprizio, M. P., Lorente, A., Borsdorff, T., Parker, R. J., and Aben, I.: Assessing methane emissions from collapsing Venezuelan oil production using TROPOMI, *EGUsphere*, 1–27, <https://doi.org/10.5194/egusphere-2023-2887>, 2023.
- 760 Naus, S., Maasakkers, J. D., Gautam, R., Omara, M., Stikker, R., Veenstra, A. K., Nathan, B., Irakulis-Loitxate, I., Guanter, L., Pandey, S., Girard, M., Lorente, A., Borsdorff, T., and Aben, I.: Assessing the Relative Importance of Satellite-Detected Methane Superemitters in Quantifying Total Emissions for Oil and Gas Production Areas in Algeria, *Environ. Sci. Technol.*, 57, 19545–19556, <https://doi.org/10.1021/acs.est.3c04746>, 2023.
- 765 Nesser, H., Jacob, D. J., Maasakkers, J. D., Scarpelli, T. R., Sulprizio, M. P., Zhang, Y., and Rycroft, C. H.: Reduced-cost construction of Jacobian matrices for high-resolution inversions of satellite observations of atmospheric composition, *Atmospheric Measurement Techniques*, 14, 5521–5534, <https://doi.org/10.5194/amt-14-5521-2021>, 2021.
- Nesser, H., Jacob, D. J., Maasakkers, J. D., Lorente, A., Chen, Z., Lu, X., Shen, L., Qu, Z., Sulprizio, M. P., Winter, M., Ma, S., Bloom, A. A., Worden, J. R., Stavins, R. N., and Randles, C. A.: High-resolution US methane emissions inferred from an inversion of 2019 TROPOMI satellite data: contributions from individual states, urban areas, and landfills, *Atmospheric Chemistry and Physics*, 24, 5069–5091, <https://doi.org/10.5194/acp-24-5069-2024>, 2024.
- 770 Parker, R. J., Webb, A., Boesch, H., Somkuti, P., Barrio Guillo, R., Di Noia, A., Kalaitzi, N., Anand, J. S., Bergamaschi, P., Chevallier, F., Palmer, P. I., Feng, L., Deutscher, N. M., Feist, D. G., Griffith, D. W. T., Hase, F., Kivi, R., Morino, I., Notholt, J., Oh, Y.-S., Ohyama, H., Petri, C., Pollard, D. F., Roehl, C., Sha, M. K., Shiomi, K., Strong, K., Sussmann, R., Té, Y., Velazco, V. A., Warneke, T., Wennberg, P. O., and Wunch, D.: A decade of GOSAT Proxy satellite CH<sub>4</sub> observations, *Earth System Science Data*, 12, 3383–3412, <https://doi.org/10.5194/essd-12-3383-2020>, 2020.
- 775 Prather, M. J., Holmes, C. D., and Hsu, J.: Reactive greenhouse gas scenarios: Systematic exploration of uncertainties and the role of atmospheric chemistry, *Geophysical Research Letters*, 39, <https://doi.org/10.1029/2012GL051440>, 2012.
- 780 Qu, Z., Jacob, D. J., Shen, L., Lu, X., Zhang, Y., Scarpelli, T. R., Nesser, H., Sulprizio, M. P., Maasakkers, J. D., Bloom, A. A., Worden, J. R., Parker, R. J., and Delgado, A. L.: Global distribution of methane emissions: a comparative inverse analysis of observations from the TROPOMI and GOSAT satellite instruments, *Atmospheric Chemistry and Physics*, 21, 14159–14175, <https://doi.org/10.5194/acp-21-14159-2021>, 2021.
- Randerson, J. T., Van Der Werf, G. R., Giglio, L., Collatz, G. J., and Kasibhatla, P. S.: Global Fire Emissions Database, Version 4.1 (GFEDv4), ORNL DAAC, <https://doi.org/10.3334/ORNLDAAC/1293>, 2017.
- Rodgers, C. D.: *Inverse Methods for Atmospheric Sounding: Theory and Practice*, WORLD SCIENTIFIC, <https://doi.org/10.1142/3171>, 2000.



- 785 Saunio, M., Stavert, A. R., Poulter, B., Bousquet, P., Canadell, J. G., Jackson, R. B., Raymond, P. A., Dlugokencky, E. J.,  
Houweling, S., Patra, P. K., Ciais, P., Arora, V. K., Bastviken, D., Bergamaschi, P., Blake, D. R., Brailsford, G., Bruhwiler,  
L., Carlson, K. M., Carrol, M., Castaldi, S., Chandra, N., Crevoisier, C., Crill, P. M., Covey, K., Curry, C. L., Etiope, G.,  
Frankenberg, C., Gedney, N., Hegglin, M. I., Höglund-Isaksson, L., Hugelius, G., Ishizawa, M., Ito, A., Janssens-Maenhout,  
G., Jensen, K. M., Joos, F., Kleinen, T., Krummel, P. B., Langenfelds, R. L., Laruelle, G. G., Liu, L., Machida, T.,  
790 Maksyutov, S., McDonald, K. C., McNorton, J., Miller, P. A., Melton, J. R., Morino, I., Müller, J., Murguía-Flores, F., Naik,  
V., Niwa, Y., Noce, S., O'Doherty, S., Parker, R. J., Peng, C., Peng, S., Peters, G. P., Prigent, C., Prinn, R., Ramonet, M.,  
Regnier, P., Riley, W. J., Rosentretter, J. A., Segers, A., Simpson, I. J., Shi, H., Smith, S. J., Steele, L. P., Thornton, B. F.,  
Tian, H., Tohjima, Y., Tubiello, F. N., Tsuruta, A., Viovy, N., Voulgarakis, A., Weber, T. S., van Weele, M., van der Werf,  
G. R., Weiss, R. F., Worthy, D., Wunch, D., Yin, Y., Yoshida, Y., Zhang, W., Zhang, Z., Zhao, Y., Zheng, B., Zhu, Q., Zhu,  
795 Q., and Zhuang, Q.: The Global Methane Budget 2000–2017, *Earth System Science Data*, 12, 1561–1623,  
<https://doi.org/10.5194/essd-12-1561-2020>, 2020.

Scarpelli, T. R., Jacob, D. J., Villasana, C. A. O., Hernández, I. F. R., Moreno, P. R. C., Alfaro, E. A. C., García, M. Á. G.,  
and Zavala-Araiza, D.: A gridded inventory of anthropogenic methane emissions from Mexico based on Mexico's national  
inventory of greenhouse gases and compounds, *Environ. Res. Lett.*, 15, 105015, <https://doi.org/10.1088/1748-9326/abb42b>,  
800 2020.

Scarpelli, T. R., Jacob, D. J., Moran, M., Reuland, F., and Gordon, D.: A gridded inventory of Canada's anthropogenic  
methane emissions, *Environ. Res. Lett.*, 17, 014007, <https://doi.org/10.1088/1748-9326/ac40b1>, 2022a.

Scarpelli, T. R., Jacob, D. J., Grossman, S., Lu, X., Qu, Z., Sulprizio, M. P., Zhang, Y., Reuland, F., Gordon, D., and  
Worden, J. R.: Updated Global Fuel Exploitation Inventory (GFEI) for methane emissions from the oil, gas, and coal sectors:  
805 evaluation with inversions of atmospheric methane observations, *Atmospheric Chemistry and Physics*, 22, 3235–3249,  
<https://doi.org/10.5194/acp-22-3235-2022>, 2022b.

Schuit, B. J., Maasackers, J. D., Bijl, P., Mahapatra, G., van den Berg, A.-W., Pandey, S., Lorente, A., Borsdorff, T.,  
Houweling, S., Varon, D. J., McKeever, J., Jervis, D., Girard, M., Irakulis-Loitxate, I., Gorroño, J., Guanter, L., Cusworth,  
D. H., and Aben, I.: Automated detection and monitoring of methane super-emitters using satellite data, *Atmospheric*  
810 *Chemistry and Physics*, 23, 9071–9098, <https://doi.org/10.5194/acp-23-9071-2023>, 2023.

Sentinel-5P Level 2 - Registry of Open Data on AWS: <https://registry.opendata.aws/sentinel5p/>, last access: 25 April 2024.

Shen, L., Zavala-Araiza, D., Gautam, R., Omara, M., Scarpelli, T., Sheng, J., Sulprizio, M. P., Zhuang, J., Zhang, Y., Qu, Z.,  
Lu, X., Hamburg, S. P., and Jacob, D. J.: Unravelling a large methane emission discrepancy in Mexico using satellite  
observations, *Remote Sensing of Environment*, 260, 112461, <https://doi.org/10.1016/j.rse.2021.112461>, 2021.

815 Shen, L., Jacob, D. J., Gautam, R., Omara, M., Scarpelli, T. R., Lorente, A., Zavala-Araiza, D., Lu, X., Chen, Z., and Lin, J.:  
National quantifications of methane emissions from fuel exploitation using high resolution inversions of satellite  
observations, *Nat Commun*, 14, 4948, <https://doi.org/10.1038/s41467-023-40671-6>, 2023.

Sheng, J.-X., Jacob, D. J., Turner, A. J., Maasackers, J. D., Sulprizio, M. P., Bloom, A. A., Andrews, A. E., and Wunch, D.:  
820 High-resolution inversion of methane emissions in the Southeast US using SEAC<sup>4</sup>RS aircraft observations of atmospheric  
methane: anthropogenic and wetland sources, *Atmospheric Chemistry and Physics*, 18, 6483–6491,  
<https://doi.org/10.5194/acp-18-6483-2018>, 2018.

Thoning, K., Dlugokencky, E., Lan, X., and NOAA Global Monitoring Laboratory: Trends in globally-averaged CH<sub>4</sub>, N<sub>2</sub>O,  
and SF<sub>6</sub>, <https://doi.org/10.15138/P8XG-AA10>, 2022.



- 825 Tsuruta, A., Kivimäki, E., Lindqvist, H., Karppinen, T., Backman, L., Hakkarainen, J., Schneising, O., Buchwitz, M., Lan, X., Kivi, R., Chen, H., Buschmann, M., Herkommer, B., Notholt, J., Roehl, C., Té, Y., Wunch, D., Tamminen, J., and Aalto, T.: CH<sub>4</sub> Fluxes Derived from Assimilation of TROPOMI XCH<sub>4</sub> in CarbonTracker Europe-CH<sub>4</sub>: Evaluation of Seasonality and Spatial Distribution in the Northern High Latitudes, *Remote Sensing*, 15, 1620, <https://doi.org/10.3390/rs15061620>, 2023.
- U.S. Greenhouse Gas Center: <https://earth.gov/>, last access: 2 May 2024.
- 830 Varon, D. J., Jacob, D. J., Sulprizio, M., Estrada, L. A., Downs, W. B., Shen, L., Hancock, S. E., Nesser, H., Qu, Z., Penn, E., Chen, Z., Lu, X., Lorente, A., Tewari, A., and Randles, C. A.: Integrated Methane Inversion (IMI 1.0): a user-friendly, cloud-based facility for inferring high-resolution methane emissions from TROPOMI satellite observations, *Geoscientific Model Development*, 15, 5787–5805, <https://doi.org/10.5194/gmd-15-5787-2022>, 2022.
- 835 Varon, D. J., Jacob, D. J., Hmiel, B., Gautam, R., Lyon, D. R., Omara, M., Sulprizio, M., Shen, L., Pendergrass, D., Nesser, H., Qu, Z., Barkley, Z. R., Miles, N. L., Richardson, S. J., Davis, K. J., Pandey, S., Lu, X., Lorente, A., Borsdorff, T., Maasakkers, J. D., and Aben, I.: Continuous weekly monitoring of methane emissions from the Permian Basin by inversion of TROPOMI satellite observations, *Atmospheric Chemistry and Physics*, 23, 7503–7520, <https://doi.org/10.5194/acp-23-7503-2023>, 2023.
- 840 Veeckind, J. P., Aben, I., McMullan, K., Förster, H., de Vries, J., Otter, G., Claas, J., Eskes, H. J., de Haan, J. F., Kleipool, Q., van Weele, M., Hasekamp, O., Hoogeveen, R., Landgraf, J., Snel, R., Tol, P., Ingmann, P., Voors, R., Kruizinga, B., Vink, R., Visser, H., and Levelt, P. F.: TROPOMI on the ESA Sentinel-5 Precursor: A GMES mission for global observations of the atmospheric composition for climate, air quality and ozone layer applications, *Remote Sensing of Environment*, 120, 70–83, <https://doi.org/10.1016/j.rse.2011.09.027>, 2012.
- 845 Watine-Guiu, M., Varon, D. J., Irakulis-Loitxate, I., Balasus, N., and Jacob, D. J.: Geostationary satellite observations of extreme and transient methane emissions from oil and gas infrastructure, *Proceedings of the National Academy of Sciences*, 120, e2310797120, <https://doi.org/10.1073/pnas.2310797120>, 2023.
- Wecht, K. J., Jacob, D. J., Frankenberg, C., Jiang, Z., and Blake, D. R.: Mapping of North American methane emissions with high spatial resolution by inversion of SCIAMACHY satellite data, *Journal of Geophysical Research: Atmospheres*, 119, 7741–7756, <https://doi.org/10.1002/2014JD021551>, 2014.
- 850 Worden, J. R., Cusworth, D. H., Qu, Z., Yin, Y., Zhang, Y., Bloom, A. A., Ma, S., Byrne, B. K., Scarpelli, T., Maasakkers, J. D., Crisp, D., Duren, R., and Jacob, D. J.: The 2019 methane budget and uncertainties at 1° resolution and each country through Bayesian integration Of GOSAT total column methane data and a priori inventory estimates, *Atmospheric Chemistry and Physics*, 22, 6811–6841, <https://doi.org/10.5194/acp-22-6811-2022>, 2022.
- 855 Yin, Y., Chevallier, F., Ciais, P., Bousquet, P., Saunoy, M., Zheng, B., Worden, J., Bloom, A. A., Parker, R. J., Jacob, D. J., Dlugokencky, E. J., and Frankenberg, C.: Accelerating methane growth rate from 2010 to 2017: leading contributions from the tropics and East Asia, *Atmospheric Chemistry and Physics*, 21, 12631–12647, <https://doi.org/10.5194/acp-21-12631-2021>, 2021.
- 860 Yu, X., Millet, D. B., Henze, D. K., Turner, A. J., Delgado, A. L., Bloom, A. A., and Sheng, J.: A high-resolution satellite-based map of global methane emissions reveals missing wetland, fossil fuel, and monsoon sources, *Atmospheric Chemistry and Physics*, 23, 3325–3346, <https://doi.org/10.5194/acp-23-3325-2023>, 2023.
- Yuan, B., Kaser, L., Karl, T., Graus, M., Peischl, J., Campos, T. L., Shertz, S., Apel, E. C., Hornbrook, R. S., Hills, A., Gilman, J. B., Lerner, B. M., Warneke, C., Flocke, F. M., Ryerson, T. B., Guenther, A. B., and de Gouw, J. A.: Airborne flux



measurements of methane and volatile organic compounds over the Haynesville and Marcellus shale gas production regions, *Journal of Geophysical Research: Atmospheres*, 120, 6271–6289, <https://doi.org/10.1002/2015JD023242>, 2015.

865 Zhang, Y., Jacob, D. J., Maasackers, J. D., Sulprizio, M. P., Sheng, J.-X., Gautam, R., and Worden, J.: Monitoring global tropospheric OH concentrations using satellite observations of atmospheric methane, *Atmospheric Chemistry and Physics*, 18, 15959–15973, <https://doi.org/10.5194/acp-18-15959-2018>, 2018.

870 Zhang, Y., Gautam, R., Pandey, S., Omara, M., Maasackers, J. D., Sadavarte, P., Lyon, D., Nesser, H., Sulprizio, M. P., Varon, D. J., Zhang, R., Houweling, S., Zavala-Araiza, D., Alvarez, R. A., Lorente, A., Hamburg, S. P., Aben, I., and Jacob, D. J.: Quantifying methane emissions from the largest oil-producing basin in the United States from space, *Science Advances*, 6, eaaz5120, <https://doi.org/10.1126/sciadv.aaz5120>, 2020.

Zhang, Z., Zimmermann, N. E., Kaplan, J. O., and Poulter, B.: Modeling spatiotemporal dynamics of global wetlands: comprehensive evaluation of a new sub-grid TOPMODEL parameterization and uncertainties, *Biogeosciences*, 13, 1387–1408, <https://doi.org/10.5194/bg-13-1387-2016>, 2016.

875